nature chemistry

SUPPLEMENTARY INFORMATION

DOI: 10.1038/NCHEM.2853

In the format provided by the authors and unedited.

Chromophore twisting in the excited state of a photoswitchable fluorescent protein captured by time-resolved serial femtosecond crystallography

Nicolas Coquelle, Michel Sliwa, Joyce Woodhouse, Giorgio Schirò, Virgile Adam, Andrew Aquila, Thomas R. M. Barends, Sébastien Boutet, Martin Byrdin, Sergio Carbajo, Eugenio De la Mora, R. Bruce Doak, Mikolaj Feliks, Franck Fieschi, Lutz Foucar, Virginia Guillon, Mario Hilpert, Mark Hunter, Stefan Jakobs, Jason E. Koglin, Gabriela Kovacsova, Thomas J. Lane, Bernard Lévy, Mengning Liang, Karol Nass, Jacqueline Ridard, Joseph S. Robinson, Christopher M. Roome, Cyril Ruckebusch, Matthew Seaberg, Michel Thepaut, Marco Cammarata, Isabelle Demachy, Martin Field, Robert L. Shoeman, Dominique Bourgeois, Jacques-Philippe Colletier, Ilme Schlichting, Martin Weik

correspondence to: martin.weik@ibs.fr, Ilme.Schlichting@mpimf-heidelberg.mpg.de, colletier@ibs.fr

Table- of- contents

1. Ultrafast transient absorption spectroscopy

Ultrafast transient absorption spectroscopy of rsEGFP2 in solution in the picosecond time-domain carried out at low pump energy

The ultrafast transient absorption experiments were carried out on rsEGFP2 in 50 mM Hepes, 50 mM NaCl, pH 8, using a method similar to that described elsewhere for IrisFP[1]. Briefly, a 1-kHz femtosecond transient absorption set up was used; and the pump beam (400 nm) was obtained by doubling fundamental 800 nm pulses. The solution of rsEGFP2 in the *off* state (absorbance ca. 0.1 at 400 nm) was inside a flow cell (1 mm thick CaF_2 windows, optical path length 250 μm). Before entering the flowcell, the reservoir solution was irradiated continuously with 470 nm light to switch the protein back to the *off* state after excitation by the pump beam (2 μJ / pulse at the sample position; spot diameter 0.4 mm; energy density 1.3 mJ/cm^2). Owing to the low absorbance and the low pump excitation power, multiphoton processes and formation of ionic species were avoided (see next section for higher-power experiments). The instrument response function (110 fs FWHM) was estimated using the stimulated Raman amplification signal (Supplementary Fig. 1a) and spectra were corrected from group velocity dispersion.

Supplementary Fig. 1a-c shows the transient difference absorbance spectra from 355 to 675 nm and from -0.1 to 39.9 ps after excitation of rsEGFP2 in its *off* state by a 110 fs pulse at 400 nm. Between -0.1 and 0.4 ps, four difference bands are growing (Supplementary Fig. 1a): two positive (maxima at 355, 455 nm) and two negative bands (narrow and broad band with minima at 405 nm and 530 nm, respectively). The former are characteristic of absorption by excited-state species, the latter reflect the depopulation of the *off* state (405 nm) and stimulated emission of excited-state species (530 nm). Between 0.5 and 39.9 ps, all bands decay with two time constants (a global decay analysis was carried out where we focused on spectral changes observed at four wavelengths (385, 455, 530 and 650 nm) and this analysis yielded two decay time constants of 0.92 ± 0.08 ps and 3.65 ± 0.15 ps, Supplementary Fig 1d) and a positive band is growing at 380 nm to reach a difference spectrum characterized by this positive band and a small negative band between 465 and 600 nm with a maximum at 502 nm (Supplementary Fig. 1c) that do not change up to upper limit of the pump-probe delay of 1 ns (not shown). The band at 380 nm is most likely due to formation of a protonated *cis* isomer in line with its presence in a spectrum recorded from rsEGFP2 in its fluorescent *on* state at pH 4 where the *cis* isomer of the chromophore is protonated (Supplementary Fig. 2). The negative

band with the maximum at 502 nm (Supplementary Fig. 1c, difference spectrum at 39.9 ps) originates from the depopulation and stimulated emission of the anionic *cis* isomer present in a residual population (about 10%) of the fluorescent *on* state (Supplementary Fig. 2).

Since the residual population (10%) of the fluorescent *on* state emits at 502 nm, *i.e.* close to the time-dependent stimulated-emission band with a maximum at 530 nm (Fig. 2a, Supplementary Fig. 1a-c), its time evolution needed to be determined. To this end, spectral changes of a solution with 100% of the rsEGFP2 molecules being in their fluorescent *on* state (anionic *cis* chromophore) were followed upon femtosecond excitation at 400 nm (Supplementary Fig. 3). The expected negative band with a maximum at 502 nm rises within a few hundred femtoseconds (Supplementary Fig. 3a), followed by a vibrational relaxation within a few picoseconds (shift and increase of the band), and then remains constant (Supplementary Fig. 3b) up to 50 ps. Consequently, the decay of the spectra in Fig. 2a on the ps time scale (decay in 0.9 and 3.7 ps) and Supplementary Fig. 1b,c is solely due to photo-dynamics of the protonated *off* state without contributions from the photo-dynamics of the anionic *on* state.

Ultrafast transient absorption spectroscopy of rsEGFP2 in solution as a function of pump energy

In the previous section, transient absorption spectroscopy was carried out at low pump energy (corresponding to 13 GW/cm^2 and less than one photon absorbed per protein) to avoid multi-photon and photobleaching processes. Since TR-SFX experiments were carried out at much higher pump energy (corresponding to nominal 400 GW/cm^2), transient absorption spectroscopy was carried out at two additional pump energies, corresponding to 68 and 140 GW/cm^2 (Supplementary Fig. 4). Excitation at higher pump energies was not possible due to laser scattering and a strong signal from the solvent (spectra with 140 GW/cm^2 were cut below 430 nm). At 13, 68 and 140 GW/cm^2, the 455 nm band (absorption of excited state species) reaches its maximum at 0.6 ps and decays with similar time constants (2.75 +/- 0.03 ps, 2.73 +/- 0.05 ps, 2.47 +/- 0.14 ps, respectively), indicating that the formation and decay of excited state species do not strongly depend on the pump energy. However, at 68 and 140 GW/cm^2 an additional species is formed within a few hundred femtoseconds that absorbs from 500 to 700 nm with a maximum at 700 nm (Supplementary Fig. 4e,f,h,i) and whose spectrum remains constant up to 1 ns (not shown). Similar pump-energy dependent experiments on Dronpa[2] and photoactive yellow protein[3] yielded a similar additional band that

has been interpreted as being due to the formation of solvated electrons and a chromophore radical cation.Importantly, the band attributed to a radical cation and solvated electron species does not evolve on the ps time scale. This means that this radical does not correspond to either of the two SFX intermediate states (models P and T, see below) whose occupancies decrease between 1 and 3 ps.

Power titration with femtosecond excitation of rsEGFP2 off-to-on photoswitching in solution

The *off*-to-*on* photoswitching efficiency with femtosecond laser excitation of rsEGFP2 in solution was investigated as a function of the laser energy density, similarly to experiments carried out on crystals of the photoactive yellow protein[4]. The experiments were carried out on a 2.5 mM rsEGFP2 solution in 50 mM Hepes, 50 mM NaCl, pH 8. The sample was sandwiched between the faces of an Infrasil cuvette with an optical path length of 50 μm. The pump beam to trigger *off*-to-*on* photoswitching (400 nm, about 150 fs pulse length, circular polarization) was obtained by using the second harmonic of a Coherent Femtosecond Amplifier (Elite). The white probe beam was obtained by a cold halogen lamp (Schott). Pump and probe beam spatial profiles at the sample position were characterized by a beam profiler camera (Spiricon) and were 380×250 μm^2 FWHM and 68×62 μm^2 FWHM, respectively. The stability of pump-probe spatial overlap was checked several times during the experiments. A LED source at 490 nm (Thorlabs) was collimated and focused on the sample (about 200 mW/cm^2) and used to prepare the *off* state before femtosecond excitation and to check the reversibility of photoswitching after femtosecond excitation.

Before pump-laser excitation, a spectrum of the *on* state (resting state) was collected, followed by illumination with the LED source at 490 nm for about 15 min in order to generate the *off* state (see Supplementary Fig. 5). The *on*- and *off*-state spectra were then used as a reference for interpreting the spectra after fs excitation.

The scheme of the experiment was as follows:

1 - spectrum acquisition (*on* state) during 5 seconds

2 - 490 nm LED illumination during 15 seconds

3 - spectrum acquisition (*off* state) during 5 seconds

4 - 400 nm femtosecond pulse

5 - spectrum acquisition during 5 seconds

6 - 490 nm LED illumination during 15 seconds

The above sequence was repeated five times at each laser energy. It was verified by calculation that protein molecules outside the pump surface cannot reach the probe surface within the time necessary to complete one cycle. The spectra acquired at steps 5 and 1 were used as a measure of the *on* state switching efficiency by fs excitation and of the reversibility of photoswitching after fs excitation, respectively (see Supplementary Fig. 5). The spectra were then fitted in the 380-525 nm wavelength range by a linear combination of the *on* and *off* reference spectra. Supplementary Fig. 5 shows the *on* and *off* reference spectra (blue and green curves, respectively), the spectrum after 400 nm fs excitation at 950 μJ/mm^2 (red curve), the result of the fitting procedure for the spectrum after 400 nm fs excitation (cyan curve), and the spectrum after 490 nm LED re-illumination (magenta curve).
The coefficients of the linear combination obtained with the fitting procedure give an estimate of the *on* and *off* state fractions at every step in the sequence. Supplementary Fig. 6 shows the fraction of *on* state after 400 nm laser excitation as a function of the energy density up to 1 mJ/mm^2. Supplementary Fig. 7 shows the sum of the fractions of *on* and *off* states after 400 nm laser excitation (left panel) and the fraction of *off* state after 490 nm LED re-illumination (right panel) in the same energy density range. Points in Supplementary Fig. 6 are averaged over several (typically five) repetitions. It is worth noting that sample concentration and thickness were chosen such as to have similar numbers of protein molecules in the excited volume and in microcrystals during the SFX experiment. This condition enables a direct comparison of the excitation conditions used during SFX experiments and the spectroscopic measurements described here.

Spectra in Supplementary Fig. 5 (red and cyan curves) and data in Supplementary Fig. 7 left panel demonstrate that the product of fs excitation is spectroscopically interpretable as a linear combination of *on* and *off* states over the entire energy-density range explored, including the one in the SFX experiment (0.94 mJ/mm^2). Data in Supplementary Fig. 6 shows that the *on*-to-*off* photoswitching efficiency is monotonic in the entire energy range, excluding the formation of a photobleached species that would lead to a decrease in *on*-state formation above a certain energy-density threshold. Spectra in Supplementary Fig. 5 (green and magenta curves) and data in Supplementary Fig. 7 right panel demonstrate that 99% on average of the product of femtosecond excitation is reversibly switchable back to the *off* state upon illumination by 490 nm LED radiation.

2. QM/MM and MD simulations

Excited state QM/MM simulations: calculation of protonation states

All QM/MM simulations described were performed starting from the crystallographic *off*-state conformation of the laser-off structure obtained in this work (see below).

Protonation states for the residues in the protein were obtained by performing Poisson-Boltzmann (PB) continuum electrostatic calculations combined with a Monte Carlo titration. These calculations were performed using the Pcetk module[5] of the pDynamo[6] program coupled to the external PB solver, extended-MEAD[7].

The initial setup of the electrostatic model was performed in CHARMM[8,9]. Molecular mechanics parameters, such as atomic charges and radii, were taken from the CHARMM force field[10] for the protein, whereas those for the neutral and anionic forms of the chromophore were adapted from the work of Reuter et al[11]. Hydrogen atoms were added to the X-ray crystallographic structure of the *off*-state structure of rsEGFP2 using the HBUILD routine in CHARMM.

Titratable residues were protonated according to their standard protonation states at pH 7. The coordinates of the added hydrogens were geometry optimized in CHARMM, whereas the coordinates of the heavy atoms were kept fixed. During the subsequent PB calculations in pDynamo, the solvent was assigned an ionic strength of 100 mM and a temperature of 300 K. To calculate the molecular surface of the protein, a solvent probe with a radius of 1.4 Å and an ion exclusion layer of 2.0 Å were used. The electrostatic potential was calculated using four focusing steps at resolutions of 2.0, 1.0, 0.5, and 0.25 Å. Each step employed a grid of 121^3 points. The Metropolis Monte Carlo method, as implemented in pDynamo[5], was used to calculate the protonation states of titratable groups. Each MC run consisted of 500 equilibration scans followed by 20000 production scans. Double moves[12] were applied for the pairs of groups whose absolute electrostatic interaction energy was calculated to be > 2.0 kcal mol^{-1}. Titration curves were calculated for a pH range between 0 and 14 at a resolution of 0.5 pH units.

At pH 7 the calculations indicated that the residues of the protein were all in their expected forms with the exception of Glu223, which was protonated. The histidines were all singly protonated with the delta-protonated forms being most stable for His3, His182, His200 and His218, and the epsilon-protonated forms for the remaining histidines, His5, His4, His26, His78, His82, His140, His149 and His170. The chromophore itself was determined to be

predominantly neutral, 85%, with the remaining 15% anionic. The populations of the cationic and zwitterionic forms of the chromophore were negligible for the whole range of pH values.

Excited state QM/MM simulations: molecular dynamics simulations

Once the predominant protonation states of the protein at pH 7 had been determined, a simulation model of the system with the chromophore in its neutral state was prepared using the VMD [13] and NAMD [14] programs. A molecular mechanical (MM) model of the protein was setup using the appropriate protonation states and the same CHARMM force field as indicated in the previous section. Using the solvate module of VMD this system was then solvated in an orthorhombic water box of approximate dimensions 62.0 × 73.7 × 71.3 $Å^3$ to ensure a layer of water of at least 10 Å on each side of the protein. In addition, K^+ cations were included to make the total system neutral. The complete model consisted of 3735 protein atoms, 10232 water molecules and 6 K^+ cations (34437 atoms in total). Standard CHARMM parameters were employed for the K^+ cations, and the TIP3P model[15] was taken for water.

In the next step, a geometry refinement of the model was performed in which the protein heavy atoms were weakly restrained to their experimental crystallographic positions using harmonic positional restraints (force constant 2 kcal mol^{-1} $Å^{-2}$). The solvent atoms and protein hydrogens were unrestrained. This refinement consisted of 1000 steps of geometry relaxation using the steepest descent method, a heating molecular dynamics (MD) simulation in which the temperature was gradually increased from 20 to 300 K at a rate of 10 K ps^{-1}, and a 10 ns MD equilibration run at 300 K. All calculations were done with the application of periodic boundary conditions and determination of the long-range electrostatic interactions using the particle-mesh Ewald method. The MD runs were carried out in the NPT ensemble under the normal pressure of 1 bar and using a time step of 2 fs.

To terminate, a 100 ps MD simulation was carried out (using the same conditions of temperature and pressure as above) in which all atoms were permitted to move freely. The relatively short duration of the simulation was employed to ensure that the protein atoms did not deviate substantially from their crystallographic positions. For the subsequent calculations, structures were saved at 2 ns and 10 ps intervals from the restrained and unrestrained MD simulations, respectively, giving 15 snapshots in all.

Excited state QM/MM simulations: method

All quantum chemical/molecular mechanical (QC/MM) simulations were done with the pDynamo program[6]. Most calculations were carried out with pDynamo's semi-empirical QC methods, although tests were also performed with density functional theory (DFT) and complete active space self-consistent field (CASSCF) molecular orbital methods using pDynamo coupled to the ORCA QC program[16].

We preceded our simulations with tests to calibrate different QC/MM models versus the rsEGFP2 system. For this we benefited from our previous extensive experience of the application of QC/MM methods to similar fluorescent proteins (see, for example[17,18]). Among other things, we examined the QC model, the number of atoms in the QC region, the number of mobile atoms for the QC/MM MD simulations, and the treatment of the QC/MM interactions.

Our final QC/MM model, which we used for the simulations presented in this paper, provided a reasonable compromise between accuracy and cost, and consisted of the following four points:

• the semi-empirical AM1 QC method[19] combined with the same CHARMM MM model for the non-QC atoms as employed for the MD simulations. We have shown previously that the AM1 semi-empirical method, in combination with a suitable configuration interaction (CI) method, provides a reasonable description of the ground and lower energy excited states of the chromophore[17,18]. Here, we employed a FOMO-CASCI approach, which has been shown by others to approximate state-averaged *ab initio* CASSCF methods well[20]. For our production runs, we employed an active space of 4 electrons in 3 orbitals, as we found that this gave results in accord with larger and more expensive CI spaces.

• a QC region comprising the chromophore with QC/MM covalent interactions treated *via* the link atom method[6]. This gave 45 QC atoms in total of which 3 were link atoms. Other QC regions that were tested included either all or various combinations of the additional groups, Gln95, Arg97, Ser164, Gln184, Glu223, and the water hydrogen-bonded to the chromophore's phenol group.

• an approximately spherical mobile region of 15 Å radius around the chromophore containing 2224 atoms. All other atoms were kept fixed at their initial positions during the dynamics although their interactions with the mobile atoms were, of course, computed. Test simulations allowing all atoms in the system to move showed no significant differences with those presented here.

• the inclusion of the full QC (electronic density and nuclear charge)/MM (partial charge) electrostatic interactions in the QC SCF/CI calculation. All the QC/MM and MM/MM non-bonding (electrostatic and Lennard-Jones) interactions were smoothed using the atom-based force switching approximation with inner and outer cutoffs of 8 and 12 Å, respectively[6].

With each QC/MM model, MD simulations were performed using either a velocity Verlet algorithm (all atoms mobile) or a Langevin algorithm with a small collision frequency of 10^{-2} ps^{-1} (immobile atoms 15 Å from the chromophore). The time step for each algorithm was 1 fs and simulations were run at a temperature of 300 K. For each electronic state, equilibration runs of, typically, 100 ps duration were carried out before production runs were started. To be clear, complete QC SCF and CI calculations were performed at each time step so that a 100 ps simulation with a 1 fs timestep required 10^5 SCF/CI energy and force calculations.

Excited state QM/MM simulations : chromophore models in vacuum

To test the QC model employed in the QC/MM simulations, the trans structure of the chromophore was extracted from the X-ray crystallographic structure of the *off*-state conformer and studied in vacuum. The geometry-optimized structure in the ground singlet state, S_0, has *tau* and *phi* angles of -1° and -42°, respectively. The non-planar *phi* angle is due to the unfavorable steric interaction between the phenol and the imidazolinone oxygen in the trans state. The vertical excitation energies to higher states are calculated to be 3.29, 4.01, 5.83 and 1.94 eV for the S_1, S_2, S_3 and T_1 states, respectively. The $S_0 \rightarrow S_1$ energy is in good agreement for that found for the neutral form of the chromophore in previous studies using a variety of semi-empirical and *ab initio* theoretical approaches[21,22].

Geometry optimization of the S_1 excited state leads to a lowest energy minimum with *tau* and *phi* angles of -88° and 0°, respectively, with an energy 2.13 eV higher than the geometry optimized form of S_0. There are also additional, higher energy minima for S_1 with planar values for *tau* and values of ± 90° for *phi* but we do not observe these in our subsequent simulations. The optimized geometry of the S_2 state resembles that of S_0 with values of -24° for both the *tau* and *phi* angles, whereas the geometry of S_3 has *tau* and *phi* angles of 42° and -72°, respectively, and a distorted imidazolinone ring. By contrast, the optimized geometry of T_1 is similar to that of S_1 with *tau* and *phi* angles of -105° and 1°, respectively, and an energy with respect to S_0 of 1.07 eV.

Excited state QM/MM simulations of the chromophore in rsEGFP2

The initial 100 ps simulation of the rsEGFP2 QC/MM system in its S_0 state yielded structures closely resembling the X-ray crystallographic *off*-state structure with *tau* and *phi* values (mean ± one standard deviation) of 2 ± 8° and -46 ± 11°, respectively. The vertical $S_0 \rightarrow S_1$ excitation energy was consistent with that observed for the chromophore model in vacuum with values of 3.30 ± 0.11 eV. This is equivalent to an absorption band maximum of 376 nm, which compares reasonably to the experimental value of 408 nm.

It is in principle possible to carry out quantum dynamical simulations to mimic light-excitation of the type that occurs in the TR-SFX experiments (see, for example[23]). However, these calculations are expensive and also sensitive to the way in which the radiation field is treated. Instead, in this work, we employed a simpler approach in which we performed simulations in the S_0 ground state of rsEGFP2 and then, at given intervals, spawned trajectories in the appropriate excited state. At the end of each excited state trajectory, the ground state simulation was resumed from its configuration at the last spawning point so as to have a continuous ground state trajectory. The switch from the ground to excited states was assumed to occur instantaneously without modification of the atomic positions and velocities.

We start with excitations to the S_1 state. Supplementary Fig. 8 (left panel) shows the change in the values of the *tau* and *phi* angles as a function of time for 100 S_1 excited state trajectories spawned at 1 ps intervals from a S_0 ground state trajectory. Each excited state trajectory was run for 2 ps. The angles change rapidly from their initial ground state values (*tau* = 4 ± 8°, *phi* = -48 ± 11°) to those of the S_1 state (*tau* = -86 ± 9°, *phi* = 16 ± 10°) with the change essentially being complete after 1 ps. Supplementary Fig. 9 shows the average structure at 1 ps calculated from these trajectories, which is in close agreement with the experimental intermediate structure determined by time-resolved serial femtosecond crystallography at the same time point (see below). Although we do not expect to obtain very accurate excited state kinetic constants from our simulations, due to the approximate nature of our dynamical approach, we nevertheless performed exponential fits for the curves in Supplementary Fig. 8 (left panel). We find that the change in *tau* is a mono-exponential process with a time constant of 0.32 ps, whereas the change in *phi* is bi-exponential with fast and slow components of 0.09 and 0.86 ps, respectively.

To estimate how the initial S_0 structures influence the excitation dynamics, we repeated the analyses of the preceding paragraph using various subsets of the excitation trajectories. The results were, in general, relatively insensitive to how the trajectories were selected. To

illustrate this, we show in Supplementary Fig. 8 (right panel) the change in the values of the *tau* and *phi* angles as a function of time for the 28 (out of 100) trajectories whose initial vertical $S_0 \rightarrow S_1$ excitation energy was within one third of the standard deviation (0.11 eV) of the average excitation energy (i.e. 3.30 ± 0.037 eV). As can be seen, the dynamics is very similar although the fluctuations at the start of the trajectory are a little larger. Exponential fits of these curves are qualitatively similar to the previous ones, with a time constant for the change in *tau* of 0.36 ps, and time constants for the change in *phi* of 0.10 and 0.60 ps. The average structures after 1 ps derived from the full (100) and reduced (28) sets of excitation trajectories are extremely similar and thus are not presented here. Surface hopping from the S_1 to the S_0 state was not permitted during these trajectories. When surface hopping was permitted by using the approximate AS3 surface hopping algorithm of Fabiano and co-workers[24] a substantial deexcitation to the S_0 state can occur during the 2 ps duration of the excitation trajectories. In contrast to the conclusions of Fabiano and co-workers, we note that the fraction of trajectories that deexcite is sensitive to the values of the parameters employed in the AS3 algorithm. However, with a choice of parameter values similar to theirs, we find that still approximately 15-20% of the excitation trajectories survive in the S_1 state at 1 ps. Observation of a twisted chromophore in Fig. 4 and Supplementary Fig. 9 is thus not an artifact from preventing surface hopping. Deexcitation to the S_0 state is rapid, with the ground state S_0 structure being recovered within about 150 fs.

In addition to the $S_0 \rightarrow S_1$ simulations, we also performed simulations from S_0 to the S_2 and S_3 states. We do not show results for these here as they generate structures which are consistent with model chromophore calculations (see above) that are far from the twisted intermediate structure observed experimentally. Likewise, we also examined the behavior of the T_1 state of the chromophore in the protein, although this is unlikely to be relevant to the experimental observations due to the short time span of the experiments (~1 ps) and the much longer time constants associated with singlet to triplet intersystem crossing (> 1 ns). Interestingly, we find that the average T_1 dynamical structure of the chromophore in the protein is actually quite close to that of the S_0 ground state despite the fact that its vacuum optimized structure resembles that of S_1.

Finally, we also performed switching simulations from S_1 to S_0, *i.e.* by carrying out a QM/MM MD simulation in the S_1 state and then periodically switching to S_0. In agreement with experiment we find that the majority of the simulations revert back to the *trans*

configuration of the S_0 ground state, although a small fraction, ~ 4%, leads to the *cis* configuration.

DFT calculations of the cationic ground-state chromophore in rsEGFP2

Quantum mechanical calculations of the cationic chromophore, generated by removal of one electron from the neutral *trans* species of the *off* state, were carried out for all geometries characterized by the values of *tau* and *phi* in the interval from -60° to +60° in steps of 30°. For each geometry, all coordinates except for *tau* and *phi* were optimized using density functional theory, with the B3LYP functional and 6-31G* basis set[25]. The energy landscape resulting from these calculations exhibits a unique minimum-energy geometry, corresponding to the planar *trans* chromophore of the *off*-state.

Excited state classical MD simulations: force field

Starting from the crystallographic *off*-state conformation of the laser-off structure obtained in this work (see below), force field molecular dynamics simulations of the protein with the neutral chromophore in the electronic ground state S_0 were first carried out to sample initial geometries for starting the excited state S_1 chromophore simulations.

The Amber 99 force field of the AMBER suite[26] was used for standard amino-acids. Concerning the chromophore, force constants of the bonded terms and van der Waals parameters were taken by analogy in the Amber force field. Equilibrium values were taken from geometries optimized at the DFT level of calculations for the S_0 state and CIS (Configuration Interaction between Singly excited states) level for the S_1 state, using the 6-31G* basis set[25]. The results are shown in Supplementary tables 1 and 2. Point charges for the S_0 and S_1 states were derived by fitting the *ab initio* electrostatic potential created by the chromophore (including the two peptide links) in the S_0 or S_1 state. Several constraints were imposed in the fitting procedure using a custom made program, as done previously by Jonasson *et al*[27]. The calculated values are shown in Supplementary table 3. Concerning the dihedral potentials of the *tau* and *phi* torsions around the ring bridging bonds, the standard form of the Amber force field was taken for the S_0 state with small force constants equal to 6 kcal/mol and 3 kcal/mol, respectively, to allow the chromophore to keep the large *phi* torsion angle (-46°) observed in the crystallographic *off*-state conformation of the laser-off structure. For the S_1 state of the neutral chromophore, we have to define a coupled potential of the *tau* and *phi* torsions as already done for the anionic form of the chromophore[27]. Quantum

mechanical calculations of the excited state of the neutral chromophore has been pointed out to be a difficult task[21,28], and only sparse quantitative information is available in the literature for the neutral excited state. Minima in the *tau*-twisted geometries (*tau* = +/- 90° and *phi* = 0) have been reported, with an energy stabilization with respect to the planar geometry of either -8 kcal/mol[29] [21] or -19 kcal/mol[30]. The minimum energy path from the *cis* planar geometry to the *tau*-twisted geometry calculated by Toniolo *et al* [29] shows a low barrier of about 1 kcal located near *tau* = 45°. No minimum along the *phi* torsion was reported. Olsen *et al*[30] have calculated the energy of a constrained geometry with *phi* = 90° and *tau* = 0°, yielding a destabilization of 13 kcal/mol with respect to the planar geometry. In this work we have calculated the energy landscape of the excited state using simply the CIS method. This was done only on a grid of points with absolute values of *tau* and *phi* smaller than 60°, since CIS in not reliable for absolute values near 90°. In order to obtain a complete grid we have added to the CIS points the two *tau* - twisted minima (*tau* = +/- 90° and *phi* = 0), with an energy stabilization equal to -8 kcal/mol[21,29]. The entire set of values was fitted by a sum of products of sine and cosine of multiples of *tau* and *phi*, as reported earlier[27]. The result is shown in Supplementary Fig. 10 together with the expression of the fitted analytical energy function. In agreement with the above-mentioned theoretical results, we find a strictly repulsive *phi* profile, and a *tau* profile between the *cis* and the *tau*-twisted geometry with a small barrier (0.7 kcal/mol) located at about 40°. The *tau* profile starting from the *trans* geometry is barrier-less and stabilized by -8 kcal/mol in the two *tau*-twisted geometries (*tau* = +/- 90° and *phi* = 0).

Concerning the remaining torsional parameters, those for the phenol ring were taken from the Amber force field. For the imidazolinone ring, no specific parameters are available in the standard force fields. However, these parameters, especially those governing the flexibility at the nitrogen N3 site linked to the rest of the protein, play an important role when simulating the overall dynamics of the chromophore within the protein. In this work we used a custom made specific torsional force field for the imidazolinone ring, comprising nine independent terms[31] : five terms for the intra-cycle dihedral angles (that imply only the five atoms of the ring) and four improper angles (all atoms of the ring, except N2). Usual ring force fields include also exo-cyclic dihedral terms (for instance O2-C2-N3-C1), so that the dynamics at a given atom site results from an inextricable combination of many terms.

The force constants were adjusted on the fluctuations of the nine angles observed in a 10 ps DFT/MD simulation of the S_0 anionic methyl-terminated chromophore (A. de la Lande,

private communication, 2011). The DFT/MD was performed using a modified version of deMon2k[32]. The resulting average geometry is planar. The DFT/MD fluctuations (Supplementary table 4) are found in the interval ~ 4 - 8° except the one for the N3 nitrogen improper torsion that takes, as expected, a much larger value (15.1°). The force constants of our specific force field and the resulting fluctuations are shown in the last two columns of Supplementary table 4. It appears that all DFT/MD fluctuations are well reproduced by the force field, particularly the higher flexibility of N3. This force field was initially tailored for the anionic S_0 chromophore. We have assumed it can also be used for the neutral chromophore since the higher flexibility of N3, as compared to the carbon atoms in the imidazolinone ring, is critical and is correctly reproduced here.

Excited state classical MD simulations : MD protocol

All amino acids were in their standard protonation state at pH 7, except for Glu223, which was protonated to allow hydrogen bonding with N2 of the chromophore. The protein was neutralized with Na^+ cations and solvated in a water box, resulting in 34474 atoms. The system was first minimized and equilibrated using the protocol described in[27].

A free dynamics simulation of 2 ns duration was run for the S_0 state at constant temperature (300 K) and pressure (1 atm). Fifty simulations of the S_1 state of 5 ps duration each were carried out starting from snapshots extracted from the second half of the free S_0 state simulation, and using a custom-made version of the PMEMD module of AMBER[27].

Excited state classical MD simulations: protein dynamics with the chromophore in S_0

The average value and the standard deviation of the dihedrals *tau* and *phi* in the ground state simulations are equal to -7° ± 10° and -38° ± 13°, respectively. Among the H-bonds linking the O2 oxygen of the imidazolinone ring of the chromophore to the OH oxygen of the phenol ring of the chromophore (O2-Arg97(NH2) / Arg97(NH2)-Gln184(OE1) / Gln184(OE1)-W17 / W17-Ser164(OG) / W17-OH) three of them appear as strong H-bonds: O2-Arg97(NH2), Arg97(NH2)-Gln184(OE1) and W17-OH. The H-bonds of the water W17 to Ser164 and to Gln184 exhibit a weaker character.

Excited state classical MD simulations: protein dynamics with the chromophore in S_1

The excited chromophore first accesses in less than 30 fs a flat area of the potential energy surface around the planar *tran*s geometry (Supplementary Fig. 10), where its average conformation is characterized by *tau* and *phi* values of -37° ± 12° and -10° ± 10°, respectively (conformation 1, Supplementary Fig. 11). Subsequently, full chromophore twisting occurs, leading to a conformation with *tau* and *phi* values of -80° ± 7° and 12° ± 8°, respectively (conformation 2, Supplementary Fig. 11). The fully twisted chromophore conformation is observed in all 50 simulations and forms in less than 1 ps in 18 of them and in less than 4 ps in the remaining 32, with an average value of 1.9 ps. The H-bond between the phenol oxygen of the chromophore and the water molecule W17 is formed in 98% of the S_0 snapshots and in 97% and 56% of the S_1 snapshots in which conformation 1 and conformation 2 are observed, respectively. Full twisting in *tau* is thus accompanied by a weakening of that H-bond.

S_0-S_1 energy gap and oscillator strengths calculated from QM and QM/MM simulations

TDDFT and semi-empirical QM calculations on a chromophore model were performed to determine the energy gaps and oscillator strengths of the principal conformations observed experimentally. Reliable theoretical values of the emission wavelength from the fully *tau*-twisted neutral S_1 chromophore calculated by Toniolo et al[29] and by Polyakov et al[21] are ~1100 nm and 953 nm, respectively, much too far from the observed 530 nm. Since no values for a conformation similar to SFX model P (*tau* and *phi* values of -37° and -10°, respectively) are available in the literature we have performed a calculation at the simple TDDFT level with the B3LYP density functional and the cc-pVTZ basis set, using the Gaussian 03 package. This level of calculation has been shown to provide a value of the absorption energy of the planar neutral chromophore[28] in good agreement with the accurate values of Polyakov et al[21]. The calculated emission wavelength for SFX model P is equal to 570 nm, not far from the observed 530 nm. The corresponding oscillator strength is 0.15, which is smaller than the one associated with the fully planar chromophore (0.66[28]).

The semi-empirical QM calculations provide similar results. Fully planar and SFX model P chromophores are characterized by energy gaps corresponding to 380 and 484 nm, respectively and oscillator strengths of 0.87 and 0.53. The oscillator strength of the fully twisted chromophore (SFX model T) is negligibly small (< 0.001) and its energy gap corresponds to an emission band of ~1500 nm.

We also analyzed the oscillator strengths for the structures in the QM/MM excited state simulations. As in the model chromophore calculations, their values are small for structures around the fully *tau*-twisted conformation of the chromophore (SFX model T). However, the structures with maximum oscillator strengths are clustered quite sharply in the region with *tau* values of ~ -40° and *phi* values of ~ -20° and with excitation energies of ~ 220 kJ/mol. The latter is equivalent to an emission of ~ 540 nm, which is red-shifted with respect to the emission for the model chromophore calculations. Although we only see a transient population of structures of this type, they correspond well to the minor conformation detected by MD simulations and to SFX model P.

In summary, it follows that the stimulated emission band with a maximum at 530 nm seen in the ultrafast transient absorption experiments originates most probably from SFX model P (near planar chromophore), but not from SFX model T (fully twisted chromophore).

3. Serial femtosecond crystallography

Protein expression and purification

The reversibly photoswitchable enhanced green fluorescent protein 2 (rsEGFP2[33]) was expressed and purified as described[34]. After cell lysis, purification of rsEGFP2 fused to an N-terminal polyhistidine tag was achieved using 100 ml of Ni-NTA affinity resin, followed by size exclusion chromatography on a HiLoad 16/600 Superdex 75 prep grade column. To obtain the large amount of protein required for these experiments, 136 cycles of size exclusion chromatography were performed in 9 days using two high-throughput Akta Xpress systems on the MP3 platform (IBS, Grenoble).

Microcrystal growth, preparation and injection

rsEGFP2 microcrystals were obtained by seeding (Woodhouse *et al*., to be described elsewhere), using crystallization conditions similar to those described in[34] which yield macrocrystals in the hanging drop vapor diffusion geometry. The final protein, precipitant, salt and buffer concentrations were ~20 mg/ml, ~2 M ammonium sulphate, 20 mM NaCl, 120 mM HEPES pH 8, respectively. Just prior to injection, rsEGFP2 microcrystals (3 × 3 × 3 μm^3 (Supplementary Fig. 12)) were centrifuged for 5 min in a 15 ml tube at 1000 g. The supernatant was removed and the pellet resuspended and diluted 25- to 50-fold with 100 mM HEPES pH 8, 2 M ammonium sulphate (sample from which the *on*-state reference data set was collected) or 2.5 M ammonium sulphate (for samples from which all other data sets were collected). A solution containing 2 - 10% (v/v) crystals was filtered through a 20 μm stainless steel filter using a sample loop and a high-performance liquid chromatography (HPLC) pump. After filtering, the crystal slurry was concentrated by centrifugation and removal of part of the supernatant. Crystal suspensions (typically 2 to 4 ml volume) were transferred into a stainless steel sample syringe installed on an anti-settling device[35] equipped with a regulated, adjustable Peltier element-cooled syringe holder. The sample temperature was 20°C. Crystals were injected into the vacuum (~0.1 millitorr) microfocus chamber of the Coherent X-ray Imaging (CXI) endstation[36] of the Linac Coherent Light Source (LCLS) at SLAC National Accelerator Laboratory using a gas dynamic virtual nozzle (GDVN) injector[37]. The GDVN featured a sample capillary of 75 μm inner diameter and was run at a flow rate of 30 μl/min. The resulting jet had a diameter ranging from 3 to 6 μm (corresponding to linear flow rates of 40 to 25 m/s, respectively), depending on the focusing helium pressure. Attempts to increase

the crystal concentration to above 8% (v/v) resulted in frequent clogging of the injector tubing or GDVN with rsEGFP2 microcrystals. To reduce the probability of clogging, tubing and nozzle were rinsed with water every 10 min for 2 min. A total of about 1g rsEGFP2 microcrystals were used during the five 12 hrs shifts during which our TR-SFX data were collected.

Pre-illumination of microcrystals to convert rsEGFP2 from the on to the off state

The absorption maxima of rsEGFP2 in its fluorescent (*on*) and its non-fluorescent (*off*) states are at 479 and 406 nm, respectively (Supplementary table 7). The resting state is the *on* state. Our goal was to study a picosecond timescale intermediate state along the *off*-to-*on* transition, requiring to switch all protein molecules in the crystal to the *off* state by pre-illumination (488 nm), before triggering the reaction with the pump laser (400 nm; see below), and probing the structure with X-ray pulses (Supplementary Fig. 13). The low primary quantum yield of the *on*-to-*off* photoswitching (0.04, Supplementary Table 7) required a large excess of photons per molecule to ensure efficient photoconversion. Pre-illumination was achieved by 488 nm laser light using a pre-illumination device (Supplementary Fig. 14)[38]. Briefly, the output beam of a CW laser (488 nm wavelength, 200 mW nominal power) was guided by a SMA optical fiber (200 μm core) to the tubing (254 μm inner diameter) connecting the sample reservoir with the GDVN. The optical fiber and the tubing were aligned with a stainless steel HPLC Tee union thereby forming an illumination cuvette, at a linear distance of 2 m upstream of the interaction zone. The transit time of a crystal under laser light within the pre-illumination region was 0.025 s. Absorption spectroscopy of microcrystals collected at the exit of the Tee union showed that crystalline rsEGFP2 was ~90% in the *off* state, and the remaining ~10% in the *on* state (Supplementary Fig. 15). At a flow rate of 30 μl/min, the delay between pre-illumination and laser pumping was 40 s, *i.e.* a time far shorter than the characteristic time of the *off*-to-*on* thermal recovery of monomeric rsEGFP2 in microcrystals (~100 min)[38]. Thus, the fraction of *off* state conformers in rsEGFP2 microcrystals presumably remains close to 90% at the interaction zone prior to laser pumping.

Femtosecond pump-laser excitation of rsEGFP2 crystals in TR-SFX experiments

Triggering photoswitching from the *off* towards the *on* state was achieved with pulses (~230 fs FWHM pulse length; 400 nm wavelength; 1.5 μJ/pulse; circularly polarized) generated by the second harmonic of a Ti:sapphire laser focused to a spot size of 40 μm × 40 μm (FWHM;

energy density 940 μJ mm^{-2} ; power density 400 GW cm^{-2}), in nearly collinear geometry with respect to the X-ray beam. The spatial overlap of the pump-laser focus with the XFEL beam at the interaction region was assessed every few hours by using a fine-grinded YAG screen in combination with a high-resolution camera monitoring the screen. Misalignments on the order of 20 – 30 μm were observed and corrected for.

SFX data collection and on-line monitoring

SFX data were collected at the CXI instrument of the LCLS (29 April – 3 May 2015; proposal LI56) operating at a repetition rate of 120 Hz, with a nominal photon energy of 9.5 keV (that is, a nominal wavelength of 1.3 Å) and an X-ray pulse length of 35 fs. The X-ray beam was focused to 1.3 μm (FWHM), with a beamline transmission of roughly 50%. The transmission was further reduced to 25% of the incident beam intensity, resulting in 0.3 mJ at the sample position. Data were acquired on the CSPAD detector[39], which was used in dual-gain mode with a low gain setting in the inner region to compensate for its relatively low dynamic range and obtain accurate measurements of both high and low resolution intensities. CASS[40,41] was used for online monitoring of the diffraction data, determination of the hit rate and resolution cutoff, and to estimate the fraction of multiple hits. Online real-time analysis was crucial to adjust the injector position and crystal concentration. In order to avoid FEL-related systematic effects (since the FEL can behave like two distinct alternating 60 Hz sources), equal amounts of pump laser-on [1] and pump laser-off [0] data were collected with non-uniform interleaving[42] in the following repetitive sequence: [1, 0, 1, 1, 0, 0, 0, 1, 0, 1, 0, 1, 0, 1, 0, 1, 1, 0].

Laser-on data were collected at nominal pump-probe delays of ~1 ps (laser-on-Δ1ps) and 3 ps (laser-on-Δ3ps). When collecting reference data (laser-off data), the pump-laser pulse was set to occur 20 ns after the X-ray pulse. A total of four data sets were collected at room temperature:

i) Reference data set: no pre-illumination, no pump-laser data allowed the determination of the structure of the rsEGFP2 resting state (fluorescent *on* state);

ii) *Laser-off* data set: pre-illumination, no pump-laser data allowed the determination of the structure of rsEGFP2 in the non-fluorescent *off* state;

iii) *Laser-on-Δ1ps* data set: pre-illumination, pump-laser data captured rsEGFP2 intermediate states, 1 ps after initiation of the *off*-to-*on* transition; and

iv) *Laser-on-Δ3ps* data set: pre-illumination, pump-laser data captured an rsEGFP2 intermediate state, 3 ps after initiation of the *off*-to-*on* transition.

Note that dataset ii) was in fact collected interleaved with dataset iii). During collection of dataset iv), however, only pump-laser-on data (light) were collected due to time constraints.

Calculation of absorbed X-ray dose

The diffraction-weighted dose[43] calculated for an rsEGFP2 crystal ($3 \times 3 \times 3\ \mu m^3$; containing 2.5 M ammonium sulphate in 39% of its volume) that is fully hit by the 1.3 μm Gaussian beam ($8x10^{10}$ photons/pulse) of CXI, was estimated with the RADDOSE3D server (http://www.raddo.se/)[44] to be 12 MGy. Note that RADDOSE3D does not yet take into account that photoelectrons escaping from a microcrystal diminish the energy deposited in the crystal, so that the absorbed dose was in effect smaller than 12 MGy. On the other hand, photoelectrons generated in the surrounding buffer within the jet may stream into the injected crystals, increasing the nominal dose.

Time-sorting diffraction images based on arrival time diagnostics

Time resolution in SFX experiments is achieved by temporally separating the 400 nm optical laser pulse (pump) from the following X-ray pulse (probe) by a well-defined, nominal pump-probe delay, in our case 1 ps or 3 ps. Due to the inherent time jitter of the FEL X-ray pulses, *i.e.*, the shot-to-shot temporal deviation from the expected periodic arrival time, and because of thermal drifts of the pump-probe synchronization, the actual and nominal pump-probe delays differ. The actual pump-probe delay was monitored by an arrival-time monitor (the so-called *timing tool*) developed at the LCLS X-ray free electron laser[45]. Briefly, the tool uses the ultrafast free-carrier generation induced by X-rays in a Si_3N_4 membrane to encode the relative arrival time of X-ray and pump-laser pulses. A pixel/time calibration was performed during the experiment and used to associate a correct time delay to every indexed diffraction pattern. The diagnostics showed that the delays were distributed around the nominal delay with a spread of about 400 fs for the (nominally 1 ps) laser-on-Δ1ps data and 250 fs for the (nominally 3 ps) laser-on-Δ3ps data. The time resolution of the experiment is in principle also affected by the group velocity mismatch between the X-ray and optical pulses. However, due to the small jet diameter at the X-ray / pump laser intersection point (3-6 μm), this effect is

limited to a few fs. By also taking into account the duration of the photolysis pulses (230 fs), we estimate an overall time resolution of ~430 fs.

Hit-finding and sorting of laser-on and laser-off data

We used NanoPeakCell[46] (https://github.com/coquellen/NanoPeakCell) to select hits, find Bragg-peaks and sort laser-on and laser-off images. NanoPeakCell hit-finding parameters were adjusted after visual inspection of the first diffraction patterns. All patterns with more than 10 pixels above the threshold value of 3000 were considered as hits – a deliberately permissive setting that was chosen to avoid missing potential hits. Laser-on-Δ1ps and laser-off hits were sorted based on the laser-state code present in the LCLS raw '.xtc' data stream. Indexing, integration and merging was performed with CrystFEL 0.6.1[47]. As this was the first use of NanoPeakCell in a time-resolved SFX experiment, the more established pre-processing software CASS[40,41] was also used in parallel for data-sorting, hit- and Bragg-peak-finding and automatic feeding to CrystFEL. The two programs yielded similar indexing, scaling and refinement statistics as well as electron density maps. For practical reasons, NanoPeakCell was chosen for the final off-line re-processing.

The overall hit rate was on average 2.5% due to the low crystal concentration required to prevent clogging of injection tubing and the nozzle (see sub-section on *Microcrystal growth, preparation and injection*). Indexing relied on the Bragg peaks found by NanoPeakCell, which on average extended to 2.18 (±0.4) Å resolution. The overall indexing rate was ~50%. Reaching such a high indexing rate was only possible after optimizing the geometry of the tiles of the CSPAD detector[42]. The sample-detector distance was also refined[48], by repeating the indexing task at various distances and selecting the distance yielding the maximal indexing rate. Distance refinement resulted in Gaussian-like distributions of all three unit-cell parameters. Integration was performed using the "*ring-nocen*" method in CrystFEL, and data were scaled and merged using the "*partialator*" module. Final data statistics, including R_{split}, signal-to-noise ratio (SNR) and CC*, are given in Supplementary table 5. The use of the scaling option in CrystFEL produced data with better merging statistics than the simple Monte-Carlo averaging, but neither did partiality refinement nor post-refinement (including partiality refinement; Supplementary table 6). A direct correlation was established between the Gaussian-like distribution of unit-cell parameters, the merging statistics and the content of difference Fourier density maps[48].

On-state and off-state structures of rsEGFP2: Data collection and refinement

Two reference datasets were collected, nominally corresponding to rsEGFP2 in the *on* and in the *off* state, respectively. Both structures were phased by molecular replacement (MR) using Phaser[49] and refinement was performed using the Phenix suite[50]. Graphic operations in real space were performed using Coot[51]. Figures were produced using PyMOL[525051] or custom-made python scripts and the matplotlib library[53]. All structure factor amplitude difference Fourier maps were Q-weighted as described[54] and produced using a custom-written CNS[55] script[56]. Briefly, Q-weighting assigns a weight to structure factor amplitude differences based on measurement errors (*sigma*), using Bayesian statistics. Q-weighting was introduced in the early days of time-resolved Laue crystallography as a means to improve the estimates of difference amplitudes and to reduce the noise in difference maps[54]. Q-weighting also increases the signal-to-noise ratio of amplitude differences from monochromatic datasets, and was shown to improve difference refinement[57] accuracy[58]. More recently, Q-weighting was used to generate extrapolated structure factors for difference refinement of a photobleached chromophore structure from synchrotron data[59] and to compute difference maps from XFEL data[60]. Despite integration of laser-off, laser-on-Δ1ps and laser-on-Δ3ps data sets at 1.7 Å resolution, Q-weighted difference Fourier maps were calculated at 1.9 Å resolution because of poor Q-weight values in the 1.7 – 1.9 Å resolution range.

rsEGFP2 *on*-state structure: the reference dataset that allowed solving the rsEGFP2 *on*-state structure was collected from rsEGFP2 microcrystals that were neither pre-illuminated at 488 nm nor irradiated with the pump laser at 400 nm. 986,178 patterns were collected, of which 105,612 (10.7%) contained hits and 34,715 (3.5%) were indexed (Supplementary table 5). The structure was phased by MR using the synchrotron cryo-crystallographic (100 K) structure of rsEGFP2 in the *on* state (PDB code 5DTX[34]) as a search model. Subsequent refinement of the *on*-state structure included iterative cycles of model adjustment in real space, and coordinates and individual B-factor refinement in reciprocal space. The statistics (R_{free}, R_{work} = 0.195, 0.167 at 1.7 Å resolution) of the final SFX *on*-state structure (Supplementary Fig. 16a, b) are comparable to those of the cryo-crystallographic structure of rsEGFP2 in the *on* state (R_{free}, R_{work} = 0.206, 0.174 [34] at 1.45 Å resolution). The two structures superimpose with an rmsd of 0.17 Å over 243 Cα atoms.

Pre-illuminated (488 nm), laser-off structure: the laser-off dataset was collected over three experimental shifts from rsEGFP2 microcrystals pre-illuminated at 488 nm, but without

pump-laser excitation at 400 nm. 3,531,773 patterns were collected, of which 132,264 (3.7%) contained hits and 65,097 (1.8%) were indexed (Supplementary table 5). A structure factor amplitude difference Fourier map was calculated between the laser-off dataset and the *on*-state reference dataset ($F_{obs}^{laser\text{-}off} - F_{obs}^{reference}$), using phases calculated from the *on*-state structure (Supplementary Fig. 17). A clear negative peak (-10.8 σ) on the *on*-state chromophore and a similarly high positive peak (+7.1 σ) around the coordinates of the *off*-state chromophore indicate that, in the laser-off data set, a large fraction (estimated at around 90%, see below) of the chromophores in the crystal have switched from the *on* to the *off* state upon pre-illumination. This observation is in line with the spectroscopic results obtained on pre-illuminated microcrystals collected at the exit of the pre-illumination device (see sub-section on *Pre-illumination of microcrystals*). The $F_o^{laser\text{-}off} - F_o^{reference}$ map illustrates that the *cis* (*on* state) to *trans* (*off* state) isomerization of the chromophore is accompanied by backbone motions from β-strand-7 residues (Tyr146 to Tyr152) and by conformational changes in the side chains of Tyr146, His149, Val151 and Thr204. These motions are qualitatively identical to those reported earlier[34].

The laser-off dataset was phased by molecular replacement using the *off*-state synchrotron structure of rsEGFP2 determined at 100 K (PDB code 5DTY[34]) as a search model. Examination of the initial $mF_{obs}^{laser\text{-}off}$-$DF_{calc}$ map revealed positive peaks (higher than 3 σ) on the *on* state conformations of Tyr146, Val151 and Thr204 side chains, and negative peaks on the *off*-state conformation of the chromophore and His149 side chain. Likewise, the $2mF_{obs}^{laser\text{-}off}$-$DF_{calc}$ map (Supplementary Fig. 18) indicated the presence of two conformers for the Tyr146 side chain. Hence, both maps were suggestive of a fraction of rsEGFP2 molecules having remained in the *on* state, in agreement with spectroscopic measurement on pre-illuminated microcrystals (Supplementary Fig. 15). The absence of a positive peak on His149 was tentatively explained by the observation that, in the *off*-state structure, two waters bind at its *on*-state position. These could compensate for the difference in electron density at His149.

We further investigated the hypothesis that pre-illuminated rsEGFP2 crystals contain both *on*-state and *off*-state conformers by including the *on*-state conformation of rsEGFP2 (*on* state SFX structure solved from the reference data set, see above) as an alternative conformation in the refinement. The relative occupancies of the *on*- and *off*-state chromophores were varied manually (from 0 to 45 % and from 100 to 55 %, respectively, by 5 % steps), and the refinement statistics and $mF_{obs}^{laser\text{-}off}$-$DF_{calc}$ maps inspected and compared. Refinement

statistics (namely R_{free} and R_{work}) would suggest that the occupancy of the *on*-state conformation is 25% in the laser-off SFX structure (Supplementary Fig. 19), but integration of $mF_{obs}^{laser\text{-}off}$ -DF_{calc} map (Supplementary Fig. 19b) reveals negative peaks on the *on*-state chromophore at occupancies higher than 10% (Supplementary Fig. 19b). Thus, one or more long–lived intermediate states, generated by the pre-illumination and invisible in the $2mF_{obs}^{laser\text{-}off}$ -DF_{calc} map, could exist that would display a different conformation of the chromophore and yet the same protein environment as the reference *on* state structure. As it was not possible to model these intermediates from electron density maps, we chose to use a starting model consisting of 90% *off* state and 10% *on* state for the refinement of the laser-off structure, in agreement with spectral measurements on pre-illuminated microcrystals collected at the exit of the pre-illumination device (Supplementary Fig. 15). Water 24, which is present in the chromophore pocket in the *on*-state structure but not in that of the *off* state[34], was also treated as an alternate conformer. Reciprocal space refinement included positional and B-factor refinement for all atoms. The resulting observable-to-parameter ratio was 1.52. The final laser-off structure displays refinement statistics (R_{free}, R_{work} = 0.176, 0.145 at 1.7 Å resolution) that are comparable to those reported for the cryo-crystallographic structure of rsEGFP2 in the *off* state (R_{free}, R_{work} = 0.224, 0.178 at 1.5 Å resolution), and the two structures superimpose with an rmsd of 0.12 Å over 233 Cα atoms. Further details regarding the SFX laser-off structure are listed in Supplementary table 5.

Of important note, it was verified that pre-illumination efficiency was constant during the three experimental shifts which were used to collect the laser-off dataset. To this end, we calculated difference Fourier maps between the laser-off dataset consisting of all data and reduced laser-off datasets produced from data collected during individual shifts only. The three maps, phased using the final laser-off structure (90% *off*, 10% *on*), show no features on the chromophore when displayed at ± 3.5 σ, and only minor peaks at ± 3 σ. Likewise, difference Fourier maps calculated between the laser-off dataset and datasets produced from one-to-one combinations of two shifts were featureless (Supplementary Fig. 20). Altogether, these maps confirm that the laser-off data from the three shifts contain similar structural information, and hence justify merging them to yield a single laser-off dataset and structure.

1-ps intermediate-state structure: data collection, modeling and refinement

The laser-on-Δ1ps dataset was collected over three experimental shifts from rsEGFP2 microcrystals that had been pre-illuminated at 488 nm, excited by a pump-laser at 400 nm, and probed after 1 ps by an XFEL pulse. Acquisition of this dataset and of the laser-off dataset was interleaved (see above). 3,531,773 patterns were collected, of which 132,464 (3.7%) contained hits and 64,620 (1.8%) were indexed (Supplementary Table 5). All patterns were merged into a single dataset referred to hereafter as the laser-on-Δ1ps dataset.

A difference Fourier map was calculated between the laser-on-Δ1ps dataset and the laser-off dataset, using phases calculated from the final laser-off model (90% *off*, 10% *on*). The $F_{obs}^{\text{laser-on-}\Delta 1ps}$-$F_{obs}^{\text{laser-off}}$ electron density map shows strong features on the chromophore and its vicinity, when displayed at ± 3.5 σ (Fig. 4a; Supplementary Fig. 21). The peaks are located around the chromophore (residue 68) and, with few exceptions that are outlined below, no peaks are observed at above ± 4 σ on the rest of the protein. Difference Fourier maps calculated from laser-on-Δ1ps datasets that were obtained using either all indexed images, images collected during individual shifts or combinations thereof, all revealed the same features (Supplementary Fig. 22). These six maps illustrate that the structural information present in the various datasets collected with a nominal pump-probe delay of 1 ps is similar, at least qualitatively (Supplementary Fig. 21). Hence, the $F_{obs}^{\text{laser-on-}\Delta 1ps}$-$F_{obs}^{\text{laser-off}}$ map calculated from all 1 ps light and dark data was chosen to inspect, model and refine structural changes of the protein at 1 ps after the pump-excitation. The clarity of this map can in part be explained by the high isomorphism between the two datasets compared (Supplementary Table 5).

Negative peaks are seen at the position of the chromophore in the *off*-state (peaks at the phenol hydroxyl OH, the imidazolinone carbonyl O2 and the methylene linker CB2 are at -9.1, -7.0 and -7.9 σ, respectively), suggesting that this conformation is depleted (see Supplementary Fig. 16c for a topology of the chromophore). A large positive peak appears nearby the imidazolinone ring of the chromophore, tipping at the linker atom CB2 (+6.0 σ). This peak highlights a reorientation of the chromophore phenol group and, by its bilobal nature, is suggestive of the presence of two states. In line with this observation, two positive peaks are seen between the *on*- and *off*-state positions of the phenol group (Supplementary Figs. 21 and 23). The $F_{obs}^{\text{laser-on-}\Delta 1ps}$-$F_{obs}^{\text{laser-off}}$ map also features peaks on residues in the immediate vicinity of the chromophore (Supplementary Figs. 21 and 23). First, a strong negative peak is seen on Wat17 (-5.4 σ), which is H-bonded to the chromophore OH in the *off*-state conformation. Also, a negative peak is seen on the side chain of Arg97 (strongest

peak: -4.0 σ) which, together with Glu223, stabilizes the imidazolinone ring of the chromophore, in both the *on*- and the *off*-state structures of rsEGFP2 (3 Å distance from NH2 to chromophore imidazolinone oxygen O3). Likewise, a negative peak is seen on Wat19 (-4.2 σ), at 2.7 Å from Glu223 (Oε1) and Asn69 (N). Negative peaks are observed on the side chains of Val151 and Phe166 (-3.2 and -3.0 σ, respectively) as well as on the main chain of Val151 (-3.2 σ). Gln95, another important residue for the stabilization of the chromophore, is also highlighted in the $F_{obs}^{\text{laser-on-}\Delta 1ps}$-$F_{obs}^{\text{laser-off}}$ map. In both the *on*- and the *off*-states, its side chain nitrogen is H-bonded to the chromophore carbonyl oxygen O3 through Wat8 (at 2.7 and 2.7 Å from the latter two). All three atoms feature negative peaks between -4.2 σ (Gln95 Oε1 and Wat8) and -4.8 σ (chromophore O3). The transition of the chromophore from the *off* to the intermediate state is accompanied by structural changes in the protein backbone, as indicated by a pair of positive and negative peaks seen on the backbone atoms of His149 (+3.2 σ and -3.4 σ). At the C-terminal end of the chromophore, pairs of negative and positive peaks are observed on the backbone carbonyl and side chain of Val69 (+4.2 σ and -3.3 σ), and on the sulphur atom of Cys71 (+4.4 σ and -4.2 σ), indicative of local changes. In addition to these, negative peaks are also seen on the backbone carbonyl oxygen atoms of residues that contribute the α-helix N-terminal to the chromophore (Supplementary Fig. 24). The height of these peaks inversly correlates with their distance to chromophore, being -5.9 σ on Leu65 (*n*-1), -3.9 σ on Thr 64 (*n*-2), and -3.3 σ on Val62 (*n*-4) and Leu 61 (n-5). Note that in Fig. 4, not all $F_{obs}^{\text{laser-on-}\Delta 1ps}$-$F_{obs}^{\text{laser-off}}$ peaks are visible, given the complex environment of the chromophore. These are yet illustrated in Supplementary Figs. 23 and 24.

The peaks observed in the $F_{obs}^{\text{laser-on-}\Delta 1ps}$-$F_{obs}^{\text{laser-off}}$ map suggest that part of the chromophores have moved away from their *off*-state position, and that an intermediate has built up, approximately mid-way between the *on*- and the *off*-state conformations of the chromophore. In order to assess whether these peaks indeed correspond to a new conformer, and not to a changed mixture of *on*- and *off*-state conformers[61], we calculated structure factor amplitudes (F_c) to 1.7 Å resolution from a model consisting of a 1:1 mixture of *on*- and *off*-state conformations and assigned to each F_c the experimental sigma value observed in the laser-on-Δ1ps dataset. From this simulated dataset, a $2mF_o$-DF_c electron density map was calculated, which shows a clear separation of the densities of the two states at 1.7 Å resolution – and not a merged single continuous peak between the two conformers. Hence, the positive $F_{obs}^{\text{laser-on-}\Delta 1ps}$-$F_{obs}^{\text{laser-off}}$ peaks observed mid-way between the *on*- and the *off*-state conformations of the chromophore most likely indicate the buildup of one (or two) intermediate(s) state(s).

These two $F_{obs}^{\text{laser-on-}\Delta 1ps}$-$F_{obs}^{\text{laser-off}}$ peaks are at similar height, *viz*. +5.4 (peak 1) and +6.3 σ (peak 2), and each is 2.8 Å away from a negative peak, covering either the *off*-state chromophore OH or Wat17 (Supplementary Fig. 25). The distance between peak 2 and the *off*-state chromophore OH is 1.5 Å, while that between peak 1 and the *off*-state chromophore CE2 is 1.1 Å. Hence, we considered two possible intermediate state models. In the first model (model P), the chromophore OH and CE1 were placed into peaks 2 and 1, respectively, but at the cost of a suboptimal fit into the peak on the imidazolinone ring (model P; Supplementary Fig. 25a, b). Wat17 was placed in a minor positive peak at 2.4 and 2.7 Å from Gln184 Nε2 and the chromophore OH, respectively. In the second model (model T; Supplementary Fig. 25c, d), we fitted the chromophore OH in peak 1 and the base of the phenol ring in the bifid peak on the imidazolinone ring. Peak 2 was accounted for by placing Wat17 at 2.7 Å distance from the chromophore OH. In this model, the chromophore displays a twisted geometry in that its imidazolinone and phenol rings are quasi perpendicular to one another – as opposed to being coplanar, as observed in the *on*- and *off*-state structures. Thus, in the two models, we initially accounted for the preservation of the H-bond between Wat17 and the chromophore OH.

After phasing by molecular replacement using the final laser-off structure (consisting of 90% *off*-state conformer and 10% *on*-state conformer) as a search model, no density was visible in the $2mF_o^{\text{laser-on-}\Delta 1ps}$ - DF_c (contoured at +1 σ) and $mF_o^{\text{laser-on-}\Delta 1ps}$ - DF_c maps (contoured at ±3 σ) that would have indicated the presence of model P or model T. Simulated maps (using calculated structure factors F_c and experimental sigma values) computed to 1.7 Å resolution from models consisting of a *i:j* mixture of the *off*-state conformation (all protein and chromophore atoms) and either model P or model T (only chromophore atoms) reveal that both intermediates would have been visible in $2mF_o^{\text{laser-on-}\Delta 1ps}$ - DF_c and $mF_o^{\text{laser-on-}\Delta 1ps}$ - DF_c electron density maps, if their occupancy had been higher than 25%. Therefore, the putative intermediate state(s) undraped by the $F_{obs}^{\text{laser-on-}\Delta 1ps}$-$F_{obs}^{\text{laser-off}}$ map is (are) presumably populated to less than 25%.

It was shown that in cases where insight into small structural changes was needed and where modeling errors for the two structures are correlated – as in the present case, difference refinement should lead to improved estimates of structural differences[57] – as compared to conventional refinement. Bayesian weighting of structure factor amplitude differences was further proposed to improve these estimates[62]. Q-weighting is one such Bayesian statistics approach, which assigns a weight to each amplitude difference based on the experimental

error (i.e. *sigma* values) of subtracted structure factors[58,57]. Here, Q-weighted difference amplitudes were used to produce extrapolated structure factor amplitudes for refinement of the laser-on-Δ1ps data set using the following formula[59] :

$$F_{extrapolated}^{laser\text{-}on\text{-}\Delta 1ps} = \alpha * Q/\langle Q\rangle * (F_{obs}^{laser\text{-}on\text{-}\Delta 1ps} - F_{obs}^{laser\text{-}off}) + F_{obs}^{laser\text{-}off} \text{ (eq. 1)},$$

where α is inversely proportional to the fraction of molecules that changed conformation and Q is the Bayesian weight retrieved through the Q-weighting procedure[54]. <Q> was 0.91 for the laser-on-Δ1ps *vs*. laser-off data. It is of important note that since Q is solely determined from comparisons of $F_{obs}/\sigma F_{obs}$ in the two datasets, all terms in this equation are experimental or based on experimental measurements, and no calculated structures factors (F_{calc}) are involved. Hence, our extrapolated structure factors are not biased by the laser-off structure. Despite integration of laser-off, laser-on-Δ1ps and laser-on-Δ3ps data sets at 1.7 Å resolution, difference refinement was carried out at 1.9 Å resolution because of poor Q-weight values in the 1.7 – 1.9 Å resolution range.

The first step in the difference refinement was to determine α. To this end, we compared the experimental $F_{obs}^{laser\text{-}on\text{-}\Delta 1ps} - F_{obs}^{laser\text{-}off}$ map with the $mF_{extrapolated}^{laser\text{-}on\text{-}\Delta 1ps}$ -DFc maps obtained from difference refinement of the *off*-state structure (*i.e.* the same structure that was used to phase the experimental $F_{obs}^{laser\text{-}on\text{-}\Delta 1ps} - F_{obs}^{laser\text{-}off}$ map) against $F_{extrapolated}^{laser\text{-}on\text{-}\Delta 1ps}$ calculated for various α values. At this stage, only rigid-body and B-factor refinement was performed, as our intention was to obtain a replica of $F_{obs}^{laser\text{-}on\text{-}\Delta 1ps} - F_{obs}^{laser\text{-}off}$ features in the $mF_{extrapolated}^{laser\text{-}on\text{-}\Delta 1ps}$ -DFc maps. We were expecting that, at the appropriate α value, the latter maps would feature peaks of the same height and at the same position than those observed in the former map (Supplementary Fig. 26) – *i.e.* a negative peak on the *off*-state chromophore, and positive peaks at the positions of models P and T. To estimate the similarity between maps, the ratio between absolute integrated positive and negative peaks (above 3.0 σ) in the $F_{extrapolated}^{laser\text{-}on\text{-}\Delta 1ps} - F_{c}^{laser\text{-}off}$ and the $F_{obs}^{laser\text{-}on\text{-}\Delta 1ps} - F_{obs}^{laser\text{-}off}$ maps was calculated for α-values ranging from 1 to 50 – corresponding to occupancies of 100 to 2 % (Supplementary Fig. 26b, c). We obtained a curve of sigmoidal appearance that started leveling of at α≈15, corresponding to a 6.7 % decrease in occupancy of *off*-state conformers (Supplementary Fig. 26c). The agreement between difference maps continued to improve in the range $15 \leq \alpha \leq 30$. Furthermore, electron density became visible in extrapolated $2F_{extrapolated}^{laser\text{-}on\text{-}\Delta 1ps} - F_{calc}^{laser\text{-}off}$ maps that

overlaid with phenol atoms of the chromophore in models P and T – although neither was included in the model that was used to phase these maps (Supplementary Fig. 26d, e). Challenged by the ability offered by the difference data to model such low occupancies, we used a second approach to estimate the occupancies of models P and T, whereby calculated structure factors were generated for two hypothetical models, consisting in i) 100 % *off*-state (F_{calc}^{dark}) and ii) a 50:50 mixture of model P and model T (F_{calc}^{light}); the negative peak on the *off*-state chromophore in this simulated F_{calc}^{light}-F_{calc}^{dark} map accounts for 100% of conversion from the dark to a light structure. Comparison of the integrated values of this peak in the simulated F_{calc}^{light}-F_{calc}^{dark} and experimental $F_{obs}^{laser\text{-}on\text{-}\Delta 1ps}$-$F_{obs}^{laser\text{-}off}$ maps also suggests a 6.9 % decrease in occupancy of *off*-state conformers in the laser-on-Δ1ps dataset.

At this point, we could safely assume that, overall, ~7% of microcrystalline rsEGFP2 monomers had departed from the *off*-state, but it remained unclear whether model P, model T or a combination thereof, offered the best model of the difference data. Therefore, we generated a model with both conformers present, and refined it against extrapolated structures factors generated with α = 15 (Supplementary Fig. 26c). Reciprocal space refinement included positional and B-factor refinement for all atoms, and occupancy refinement for model P and model T chromophores. Occupancies of the latter were respectively refined to 0.6 and 0.4, suggesting that, in the difference data, the two conformers co-exist. At α = 15, relative occupancies of 0.6 and 0.4 correspond to absolute occupancies of ~4 % and ~3 % for model P and model T, respectively. Note that in control calculations, the occupancies of model P and model T did not vary much as a function of α (Supplementary Fig. 26f). From there on, refinement was straightforward, and included real space fitting of residues in the $2F_{extrapolated}^{laser\text{-}on\text{-}\Delta 1ps}$ - F_{calc} electron density map. Standard equilibrium restraints (including bond, angle, torsion angle and separate planarity restraints for the imidazolinone and phenol groups) were used in the crystallographic refinement – *i.e.*, the same restraints that were used for the refinement of the static *off*- and *on*-state structures. Residues that showed conformational changes were modeled in alternate conformation, which we hypothesized to be associated to model T (and not to model P) and whose occupancy were set accordingly, due to the stronger dissimilarity of this model with the *off*-state structure (see below). R_{free}/R_{work} of the final model are 0.293/0.275 at 1.9 Å resolution.

The chromophore in model P displays a conformation close to the *off*-state chromophore, and the C2-CA2-CB2-CG2 (*tau*) and CA2-CB2-CG2-CD2 (*phi*) dihedral angles change by -

50° and +52°, respectively. The chromophore conformation in model T, however, displays an imidazolinone ring that is nearly perpendicular to that of the phenol group (Fig. 4c, d), as illustrated by respective changes in *tau* and *phi* of -84° and +43°, with respect to the *off*-state (Fig. 4c, d). We hypothesize that the similarity of model P to the *off*-state chromophore indicates that no major conformational changes in the protein scaffold accompanies the slight change in chromophore conformation. Consequently, conformational changes in the difference-refined laser-on-Δ1ps structure with respect to the *off*-state structure are interpreted as accompanying chromophore twisting towards model T. The most notable conformational change is that occurring in the side chain of Thr204 (β-strand-10), which rotates by 120° in model T (Supplementary Fig. 23). Hence, the *on*-state, the *off*-state and model T are each associated to a specific rotamer of Thr204. In model T, the chromophore phenol OH is at 2.9 and 3.1 Å from Wat356 and Wat17, respectively. Wat17 is H-bonded to Gln184(Nε1) and Ser164(Oγ) in both the *off*-state structure and in model P. As Ser164Oγ is itself a donor in the H-bond it forms with Tyr52(O), the chromophore OH is an obligate donor in the H-bond it establishes with Wat17 in the *off*-state. The same applies to Wat356, which is H-bonded to His149(O), Val151(N) and Leu202(O) and Thr204(OH) in the *off*-state structure of rsEGFP2. Upon transition of the chromophore to model T, steric hindrance forces Thr204 side chain to rotate by 120°, resulting in the breaking of its H-bond with Wat356, and in the latter becoming available for H-bonding to the chromophore phenol-OH. Upon transition to model T and formation of this H-bond, that with Wat17 is forced to break, since the chromophore OH can only be donor in a single H-bond. Thus, this water was kept in model P, but not in model T (Supplementary Fig. 23). Also due to steric hindrance, His149 side chain draws back from the chromophore phenol, but no rotation of its side chain is suggested by the data. Around the imidazolinone ring of the chromophore, side chains of several residues display conformational changes, including Leu43 (β-strand-3), Gln95, Arg97 (β-strand-5) and Glu223 (β-strand-11). Minor conformational changes are also observed in residues Val151 (β-strand-7) and Phe166 (β-strand-8).

A distance difference matrix (DDM) was calculated between the difference refined laser-on-Δ1ps structure and the *off*-state conformer (Supplementary Fig. 27a). This DDM illustrates that in addition to the above-described local-changes, the β-barrel expands upon the transition from the *off*-state to model T, and thus offers a peek into concerted conformational changes across the protein. Most notably, β-strands-7 and -10 draw away from the rest of the structure and from the chromophore (Supplementary Fig. 27a, b).

Difference Fourier maps calculated with data collected after a 3 ps pump-probe delay

The laser-on-Δ3ps dataset was collected during three hours from rsEGFP2 microcrystals pre-illuminated at 488 nm, excited by a pump-laser at 400 nm, and probed after 3 ps by XFEL pulses. 822,721 patterns were collected, of which 34,750 contained hits and 22,259 were indexed (Supplementary Table 5). Due to time constraints, we did not interleave the collection of this dataset (laser-on-Δ3ps) with that of a laser-off dataset (cf. section *SFX data collection and on-line monitoring*) but instead used as a reference dataset, the laser-off dataset collected along with the laser-on-Δ1ps dataset. This choice was justified because the pre-illumination setup was stable during the three experimental shifts used for collection of the laser-on-Δ1ps dataset, resulting in similar levels of *on*-to-*off* photoswitching efficiency. Indeed, difference Fourier maps calculated between the laser-off dataset and reduced laser-off datasets produced on a per-shift basis or from one-to-one combinations of shifts, were essentially featureless (see Supplementary Fig. 20).

The $F_{obs}^{\text{laser-on-}\Delta\text{3ps}}$-$F_{obs}^{\text{laser-off}}$ map was computed using phases calculated from the laser-off structure (consisting of 90% *off*-state and 10% *on*-state conformer). For a valid comparison, we generated a reduced laser-on-Δ1ps dataset, by randomly selecting as many indexed patterns in the laser-on-Δ1ps data, as recorded for the laser-on-Δ3ps dataset (*i.e.* 22,262 patterns). This dataset is hereafter referred to as laser-on-Δ1ps-random dataset (Supplementary Table 5) and was used to compute a $F_{obs}^{\text{laser-on-}\Delta\text{1ps-random}}$-$F_{obs}^{\text{laser-off}}$ map. As expected, features in this map are weaker than in the $F_{obs}^{\text{laser-on-}\Delta\text{1ps}}$-$F_{obs}^{\text{laser-off}}$ map, and hence better visualized at a contour level of ± 3.0 (instead of ± 3.5 σ for the $F_{obs}^{\text{laser-on-}\Delta\text{1ps}}$-$F_{obs}^{\text{laser-off}}$ map). The two maps are nevertheless qualitatively similar, showing negative peaks on the *off*-state chromophore (strongest peaks at -10.9 vs. -6.7 σ, in the $F_{obs}^{\text{laser-on-}\Delta\text{1ps}}$-$F_{obs}^{\text{laser-off}}$ and $F_{obs}^{\text{laser-on-}\Delta\text{1ps-random}}$-$F_{obs}^{\text{laser-off}}$ maps, respectively) and Wat17 (-6.4 vs. -4.5 σ), and positive peaks on the model T chromophore (5.4 vs. 4.0 σ) and model P chromophore (6.3 vs. 4.5 σ).

The $F_{obs}^{\text{laser-on-}\Delta\text{3ps}}$-$F_{obs}^{\text{laser-off}}$ map differs significantly from the two laser-on-Δ1ps maps (Fig. 4; Supplementary Fig. 28 and 29). Both the negative peak observed on the *off* state chromophore and the positive peaks on the chromophore models P and T are lower in the $F_{obs}^{\text{laser-on-}\Delta\text{3ps}}$-$F_{obs}^{\text{laser-off}}$ map (Supplementary Fig. 28 and 29). The large positive peak observed on the imidazolinone ring (peaking at 5.9 σ on the CB2 atom) in the $F_{obs}^{\text{laser-on-}\Delta\text{1ps-random}}$-$F_{obs}^{\text{laser-off}}$ map is strongly diminished. Likewise, positive peaks on the phenol-OH of model P and model T

are respectively at 2.4 and 3.9 σ in the $F_{obs}^{\text{laser-on-}\Delta 3ps}$-$F_{obs}^{\text{laser-off}}$ map, to compare to 4.5 and 4.0 σ in the $F_{obs}^{\text{laser-on-}\Delta 1ps\text{-random}}$-$F_{obs}^{\text{laser-off}}$ map. It is thus likely that model P, which was populated to 60% in the difference-refined laser-on-Δ1ps structure, has nearly vanished at 3 ps. To estimate by how much the population of model T evolves between 1 and 3 ps, we integrated peaks around the chromophore in the $F_{obs}^{\text{laser-on-}\Delta 3ps}$-$F_{obs}^{\text{laser-off}}$ map (*i.e.*, all positive peaks on the chromophore were assigned to model T), and compared this value to 40% (occupancy of model T in the difference-refined laser-on-Δ1ps structure) of that obtained from the integration of peaks around model T and model P in the $F_{obs}^{\text{laser-on-}\Delta 1ps\text{-random}}$-$F_{obs}^{\text{laser-off}}$ map. Doing so, we found that model T decreases by 44 % (Supplementary Fig. 28b, c). In line with the decrease in occupancy of the intermediate states (-100% and -44 % for model P and model T, respectively), a 37% decrease is observed of the integrated value of negative peaks around the *off*-state chromophore, when the $F_{obs}^{\text{laser-on-}\Delta 1ps\text{-random}}$-$F_{obs}^{\text{laser-off}}$ and the $F_{obs}^{\text{laser-on-}\Delta 3ps}$-$F_{obs}^{\text{laser-off}}$ are compared, suggesting that at least a fraction of the intermediate states have fallen back to the *off*-state. In addition, positive peaks are seen in the $F_{obs}^{\text{laser-on-}\Delta 3ps}$-$F_{obs}^{\text{laser-off}}$ map, which overlay with the position of the *on*-state chromophore (peaks at 4.8, 3.7 and 3.2 σ on CB2, OH and CG2) and are absent in the $F_{obs}^{\text{laser-on-}\Delta 1ps\text{-random}}$-$F_{obs}^{\text{laser-off}}$ map. Thus, the crystallographic evidence suggests that a fraction of the intermediate states have progressed towards the *cis* conformation – hence completing isomerization.

Further insight into intermediate-state conformations and occupancies at 3 ps could have been obtained from difference refinement. Due to the lower quality of the laser-on-Δ3ps dataset, however, the agreement between difference maps is lower and shows a noisier evolution as a function of α, than observed with the laser-on-Δ1ps datasets (Supplementary Fig. 26c). Thus, we refrained from further pursuing difference refinement of the 3ps dataset, and restrained ourselves to a qualitative description of features in the $F_{obs}^{\text{laser-on-}\Delta 3ps}$-$F_{obs}^{\text{laser-off}}$ map (Supplementary Fig. 28 and 29).

4. Site-directed mutagenesis, purification and spectroscopic characterisation of rsEGFP2 and rsEGFP2-V151A

The primer for V151A substitution in rsEGFP2 (5′-CAACAGCCACAACGCCTATATCATGGCC-3′) was 5’-phosphorylated with 10 U of T4 polynucleotide kinase (New England Biolabs, Ipswich, USA). PCR was carried out in a 50-µl mixture using 1 U of Q5 Hot Start High-Fidelity DNA Polymerase (New England Biolabs)

and 20 U of 9°N DNA Ligase (New England Biolabs). Digestion of the template methylated DNA was achieved by incubating the PCR product with 10 U *Dpn*I (New England Biolabs) at 37°C for 1 h. Then the sample was subjected to two more PCR cycles, ensuring the polymerisation of the reverse strand from digested fragments as primers. Competent *E. coli* DH5α cells were transformed by the final product (5 µL/50 µL cells) for DNA minipreps and sequencing. Fluorescent proteins (rsEGFP2 and rsEGFP2-V151A) fused to an N-terminal polyhistidine tag were expressed in *E. coli* BL21 (DE3) grown in an auto-inducible medium. After cell lysis, the fluorescent proteins were purified by Ni-NTA affinity chromatography.

Absorption spectra were recorded using a Jasco V-630 UV/VIS photospectrometer (Easton, USA). Emission spectra were measured with a CCD-based spectrometer (AvaSpec-ULS2048, Avantes, Eerbeek, The Netherlands) coupled with optic fibres to a cuvette holder. Photoinduced fluorescence switching cycles were measured as described[34] at low laser power densities: 6.7 mW/cm² at 488 nm (to both excite and switch-off fluorescence) and 1 mW/cm² at 405 nm (to promote *off*-to-*on* photoswitching). Photoswitching quantum yields were calculated by a custom-made routine in MATLAB (The MathWorks Inc., Natick, Massachusetts, USA) following a method reported earlier[63]. Briefly, a kinetic model involving one-to-one reversible conversion between the *on* and the *off* state was used to fit photoswitching raw data (Supplementary Fig. 30). Molar extinction coefficients of *on* and *off* states (Supplementary Table 7) were calculated using the Ward method[64].

Supplementary figures

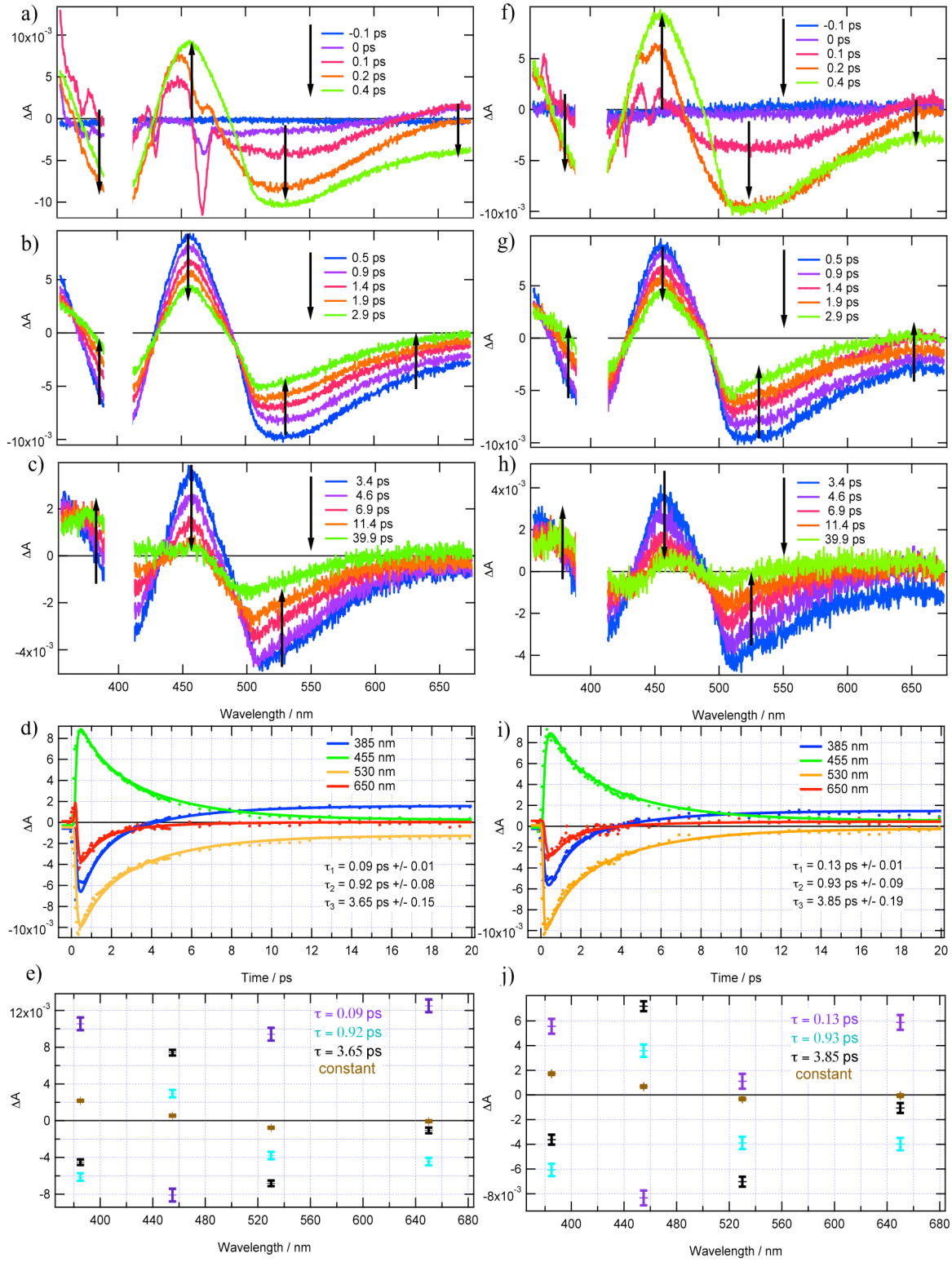

Supplementary Figure 1: Ultrafast transient difference absorption spectra of rsEGFP2 (*trans* protonated *off* state) in H_2O (a - d) and D_2O (f - i) under continuous irradiation at 470 nm at

pH 8/pD 8 recorded after excitation by the 400 nm femtosecond pulse (a, f) from -0.1 to 0.4 ps, (b, g) from 0.5 to 2.9 ps, (c, h) from 3.4 to 39.9 ps, (d, i) global fitting with four wavelengths using three exponential functions and a constant convoluted with a Gaussian pulse of 110 fs (FWHM; energy density 1.3 mJ/cm^2) and (e, j) pre-exponential factors associated to the kinetics at 385, 455, 530 and 650 nm.

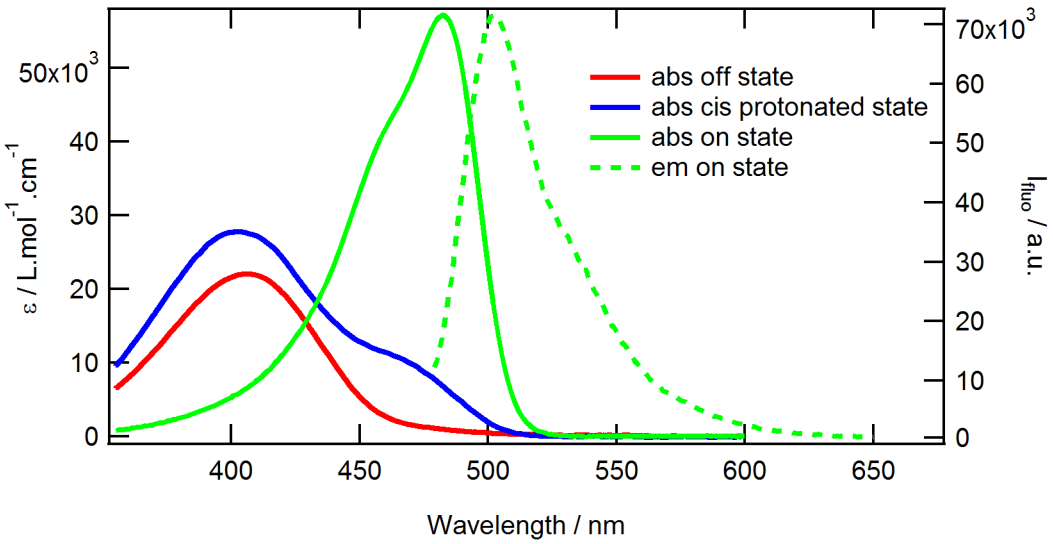

Supplementary Figure 2: Steady state absorption spectra (molar absorptivity) of rsEGFP2 in its *off* state at pH 8 (red), its *on* state at pH 4 (blue), its *on* state at pH 8 (green) and emission spectrum (excitation at 465 nm) of rsEGFP2 *on* state at pH 8 (green dashed line).

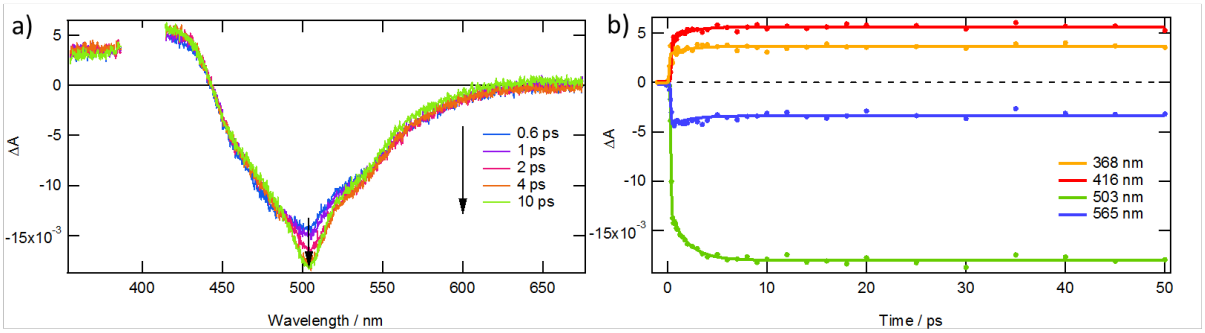

Supplementary Figure 3: (*a*) Ultrafast transient difference absorption spectra of rsEGFP2 (*cis* anionic *on* state) in solution at pH 8 recorded after excitation by a 400 nm femtosecond pulse from 0.6 to 10 ps. (*b*) Examples of the kinetics at four different wavelengths and their respective fit obtained by a global analysis with one exponential function (1.78 ps +/- 0.17 ps, vibrational relaxation) and a constant convoluted with a Gaussian pulse of 166 fs (FWHM).

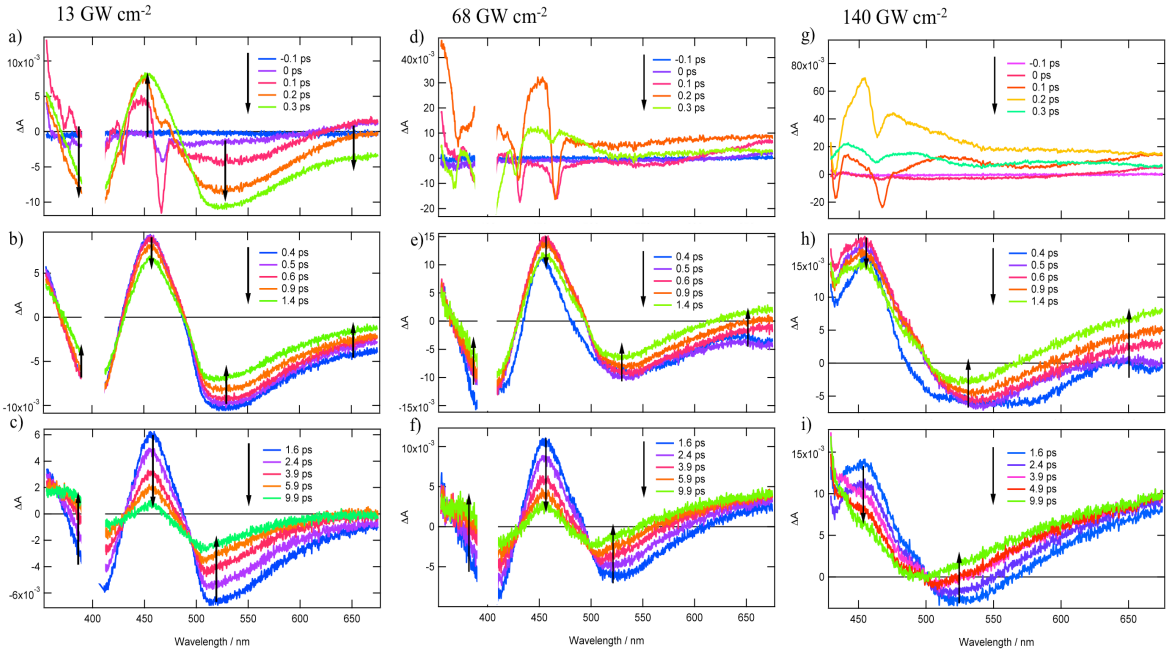

Supplementary Figure 4: Ultrafast transient difference absorption spectra of rsEGFP2 (*off* state) in H_2O under continuous irradiation at 470 nm at pH 8 recorded after excitation by a 400 nm femtosecond pulse from -0.1 to 0.3 ps (a, d, g), from 0.4 to 1.4 ps (b, e, h), and from 1.6 to 9.9 ps (c, f, i) for three different pump power densities (13 GW cm^{-2} (left), 68 GW cm^{-2} (middle), and 140 GW cm^{-2} (right).

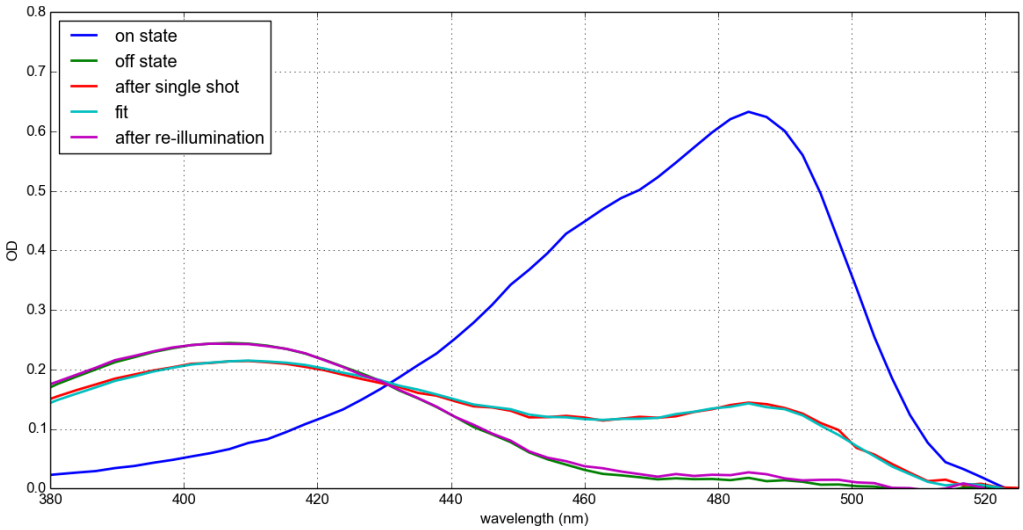

Supplementary Figure 5: *On* and *off* reference spectra (blue and green curves, respectively), spectrum after 400 nm femtosecond excitation of the *off* state at 950 μJ/mm^2 (red curve) and result of the corresponding fit (cyan curve), and spectrum after 490 nm LED re-illumination (magenta curve).

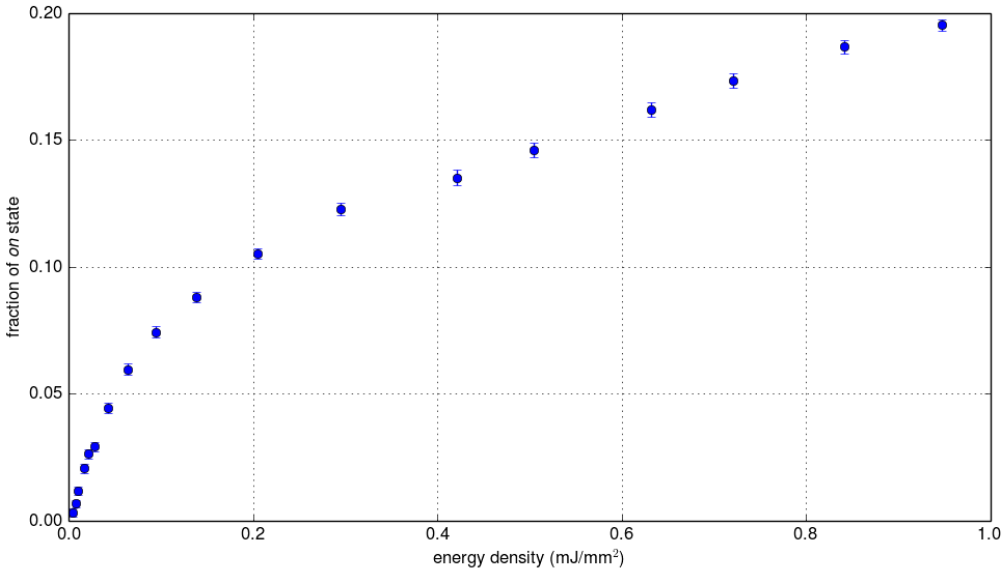

Supplementary Figure 6: Fraction of *on* state after 400 nm laser excitation as a function of the energy density in the range 0-1 mJ/mm^2. Points are averaged over several (typically 5) repetitions.

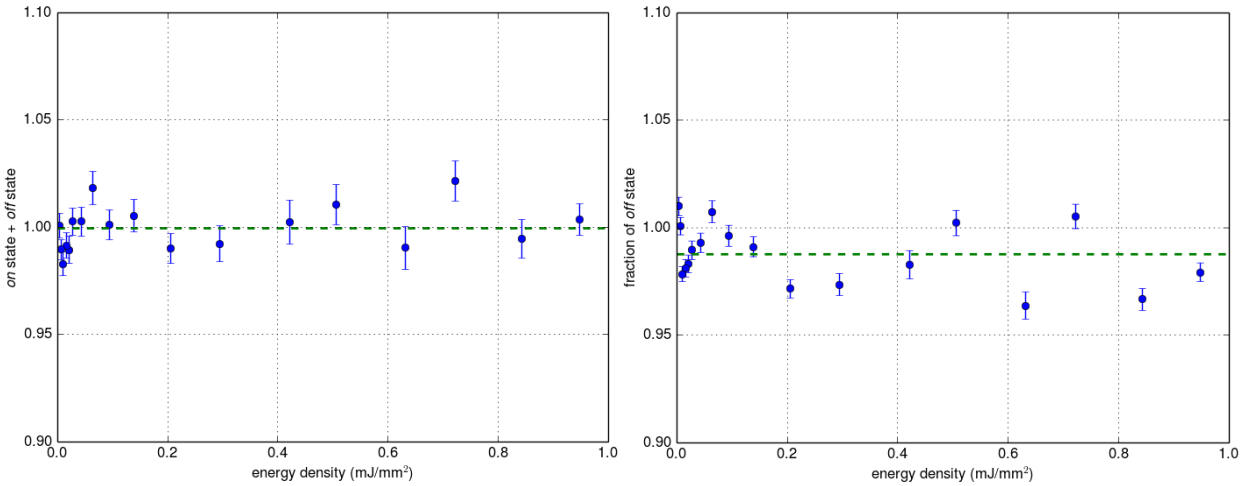

Supplementary Figure 7: Left panel: sum of the fractions of *on* and *off* states after 400 nm laser excitation as a function of the energy density in the range 0-1 mJ/mm^2. Right panel: fraction of *off* state after 490 nm LED re-illumination in the same energy density range. Points in both plots are averaged over several (typically 5) repetitions. Dashed green lines indicate the mean value of all points in every plot.

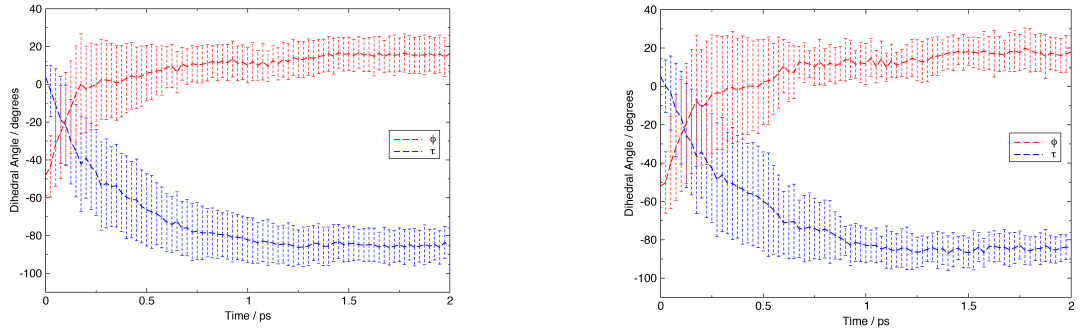

Supplementary Figure 8: The change in the *tau* (τ, blue) and *phi* (ϕ, red) dihedral angles of the chromophore in rsEGFP2 upon excitation to S_1 as a function of time obtained from QM/MM simulations. The curves correspond to the mean values calculated from the structures of 100 $S_0 \rightarrow S_1$ excitation trajectories; the error bars indicate one standard deviation on either side of the mean (left panel). The right panel shows results from a subset of 28 (out of 100) trajectories. These were selected because they had starting structures whose vertical $S_0 \rightarrow S_1$ excitation energy was within one third of a standard deviation of the average excitation energy. Note that surface hopping from the S_1 to the S_0 state was not permitted during these trajectories.

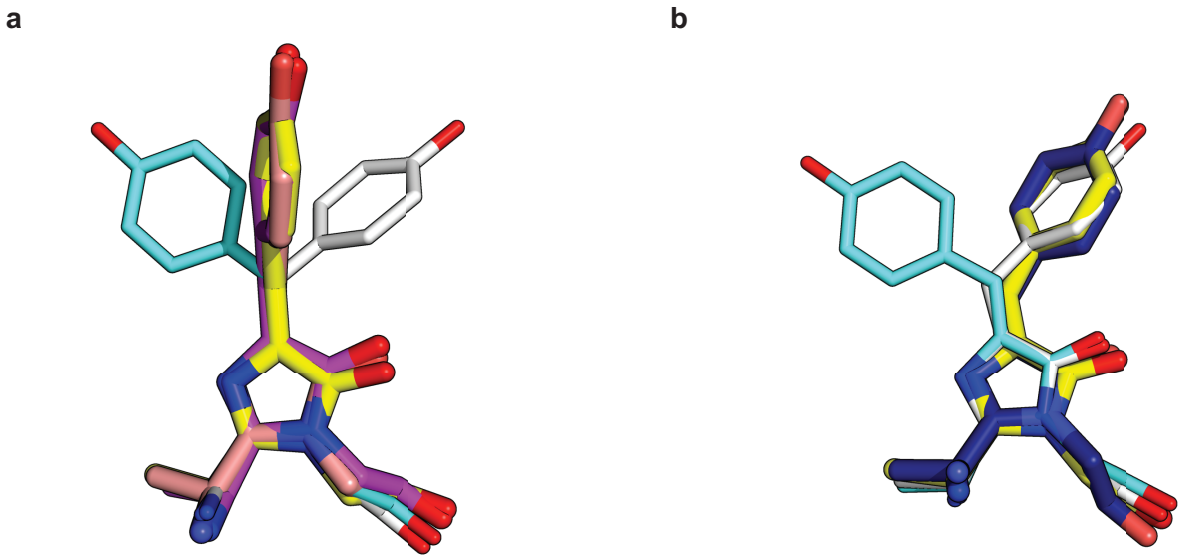

Supplementary Figure 9: Chromophore conformations determined by TR-SFX, excited-state QM/MM and excited-state classical MD simulations. (*a*) Chromophore conformation averaged over 100 S_1 QM/MM excited-state trajectories at 1 ps (magenta), superimposed with the chromophore conformation in the *off* (white), *on* (cyan) and the 1 ps intermediate state corresponding to model T (salmon) determined by TR-SFX. The major conformation found for S_1 by MD is shown in yellow. (*b*) The minor conformation found for S_1 by MD (yellow) is superimposed with the chromophore conformation in the *off* (white), *on* (cyan) and the 1 ps intermediate state corresponding to model P (blue) determined by TR-SFX.

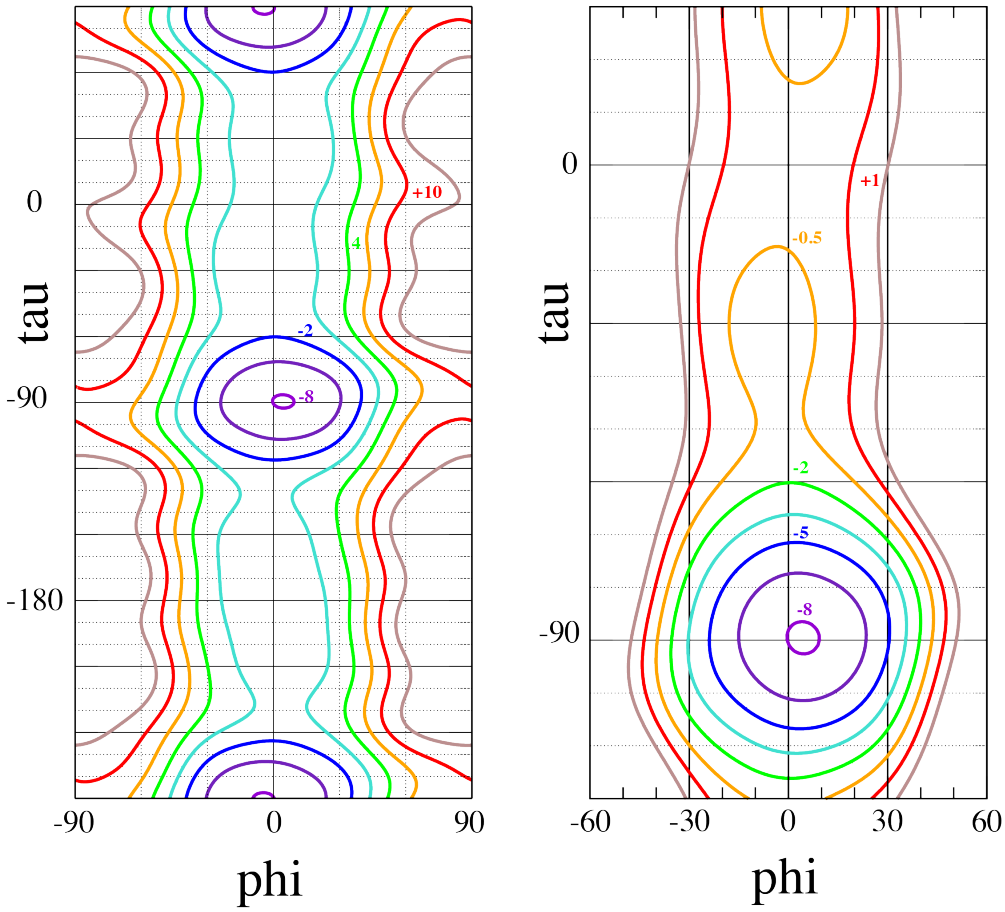

Supplementary Figure 10 : Energy landscape of the excited neutral chromophore in vacuum as a function of *phi* and *tau*. Energy values (kcal/mol) are indicated on the energy contour lines. The energy reference is that of the *trans* planar geometry (*phi* = *tau* = 0°). (left panel) landscape of the entire domain. (right) zoom on the domain explored in the present simulations. Analytical expression of the energy surface : E = 6.093 - 8.821*cos(2 ϕ) - 0.524*cos(2 ϕ) cos(τ) + 0.547*cos(6 ϕ) + 2.717*cos(2 τ) - 2.091*cos(4 τ) + 0.635*cos(6 τ) + 0.604*cos(τ) + 0.673*sin(2 ϕ) sin(3 τ) - 0.701*cos(2 ϕ)cos(3 τ) - 0.680*sin(2 ϕ) sin(8 τ) + 0.4188*sin(4 ϕ) sin(8 τ) + 0.370*cos(2 ϕ)cos(6 τ) + 0.214*sin(4 ϕ) sin(3 τ) - 0.203*cos(2 ϕ)cos(5 τ) + 0.142*cos(3 τ)

Note that in this expression ϕ is identical to *phi*, and τ is defined as the dihedral N2-CA2-CB2-CG2 (τ = *tau* + 180°).

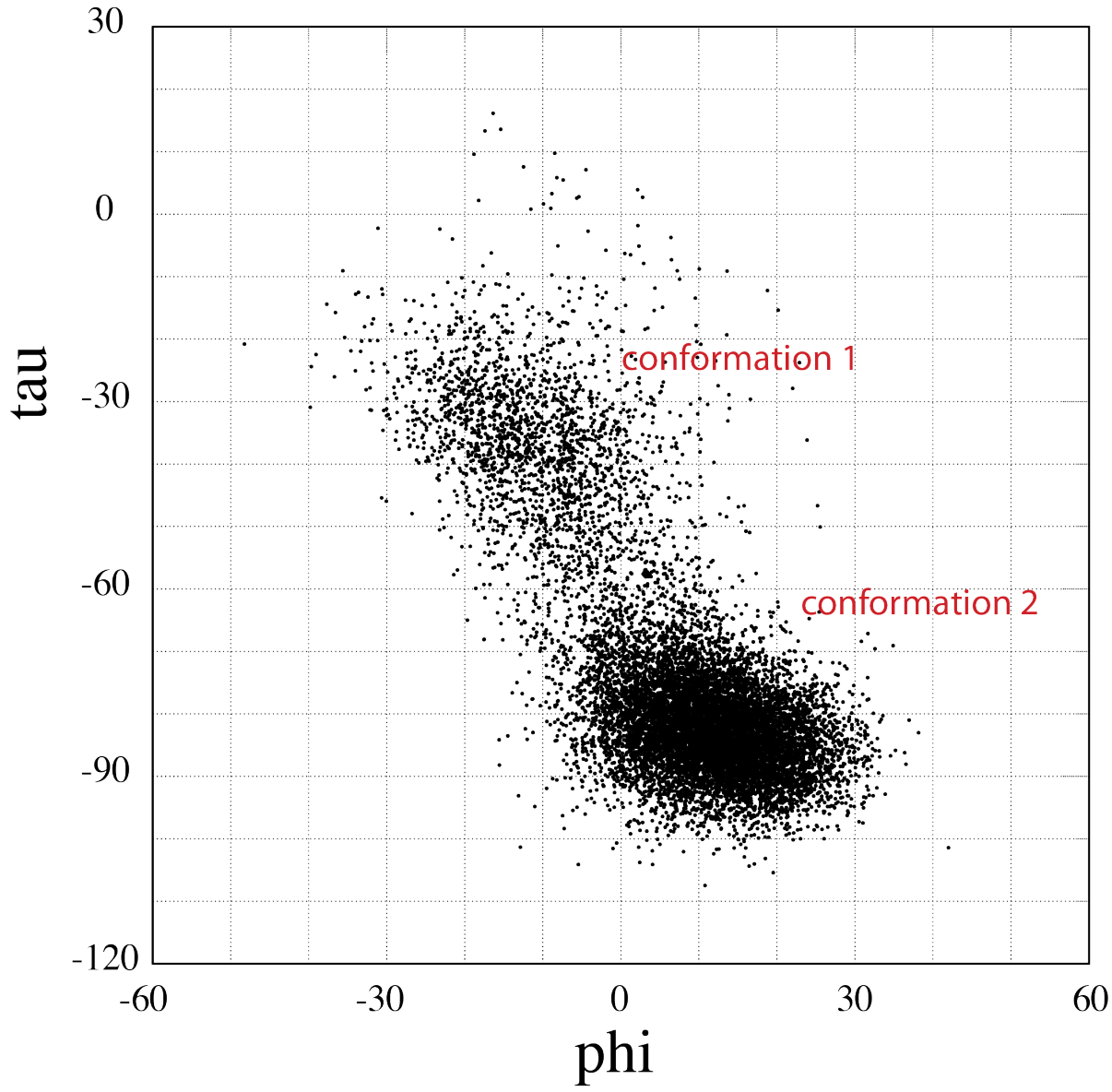

Supplementary Figure 11: Chromophore dihedral angles *tau* and *phi* observed in the first 5 ps of 50 S_1 simulations of rsEGFP2.

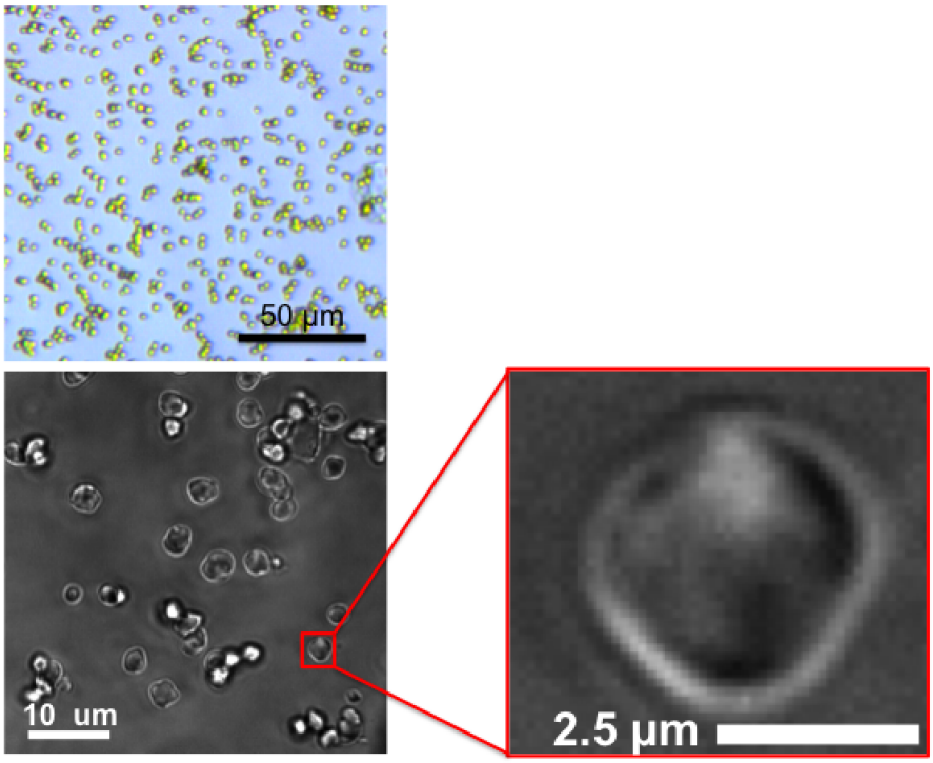

Supplementary Figure 12: Microcrystals (3 × 3 × 3 μm^3) of rsEGFP2 grown by seeding have a homogeneous size distribution. Micrographs were obtained with an optical microscope (Zeiss SteREO Discovery.V12) carrying an Achromat S 1.5 x objective (upper panel) and an inverted microscope (Olympus IX 81) with oil immersion and a total magnification of 150-fold (lower panels).

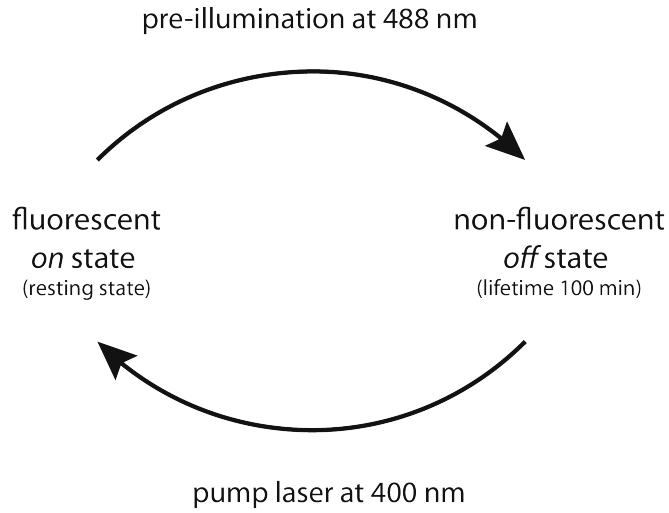

Supplementary Figure 13: rsEGFP2 microcrystals are photoswitched from the fluorescent *on* state (resting state) to the non-fluorescent *off* state (lifetime 100 min in microcrystals[38] by pre-illumination with 488 nm laser light. Pump-laser illumination at 400 nm triggers photoswitching from the *off* to the *on* state.

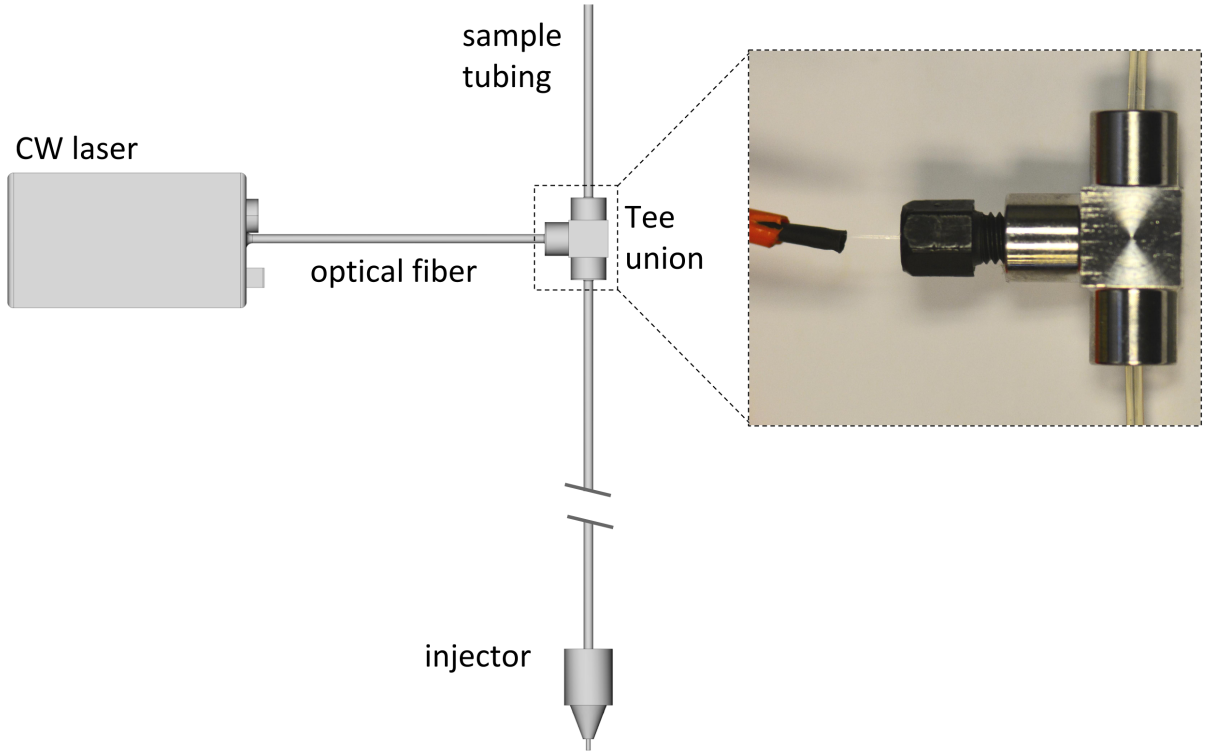

Supplementary Figure 14: Pre-illumination setup used for switching rsEGFP2 from the *on* to the *off* state[38]. A HPLC stainless steel Tee union was used to keep the polished core of a 200 μm optical fiber in place and in direct contact with the side of the tubing (ID 254 μm), through which the protein crystals were pumped. The other end of the optical fiber was connected to a 200 mW CW laser (488 nm). The protective sleeve of the optical fiber was pulled back in the photo to show the fiber core.

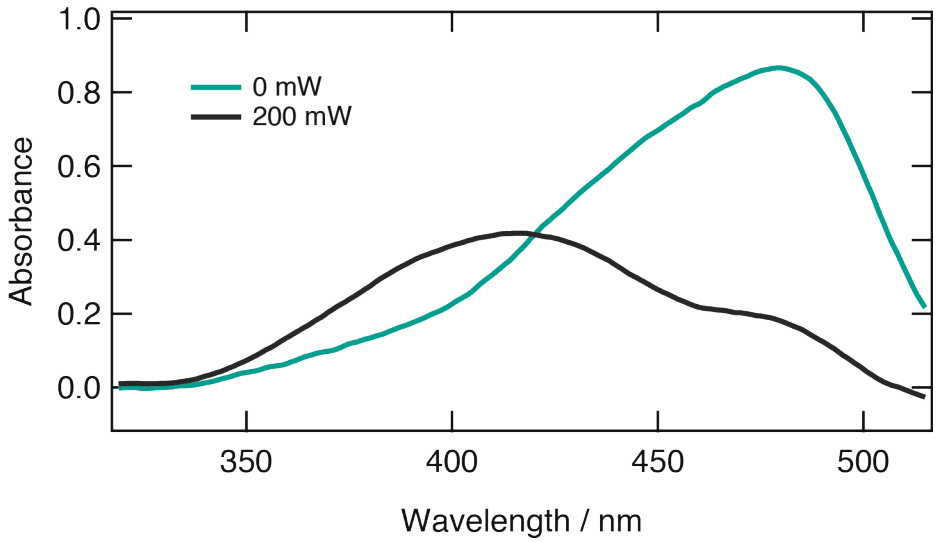

Supplementary Figure 15: Absorption spectra of rsEGFP2 microcrystals without (green) and with 488 nm pre-illumination at 200 mW (black). Calculations based on these data indicate that 90% of crystalline rsEGFP2 has been converted to the non-fluorescent *off* state, and 10% remains in the fluorescent *on* state.

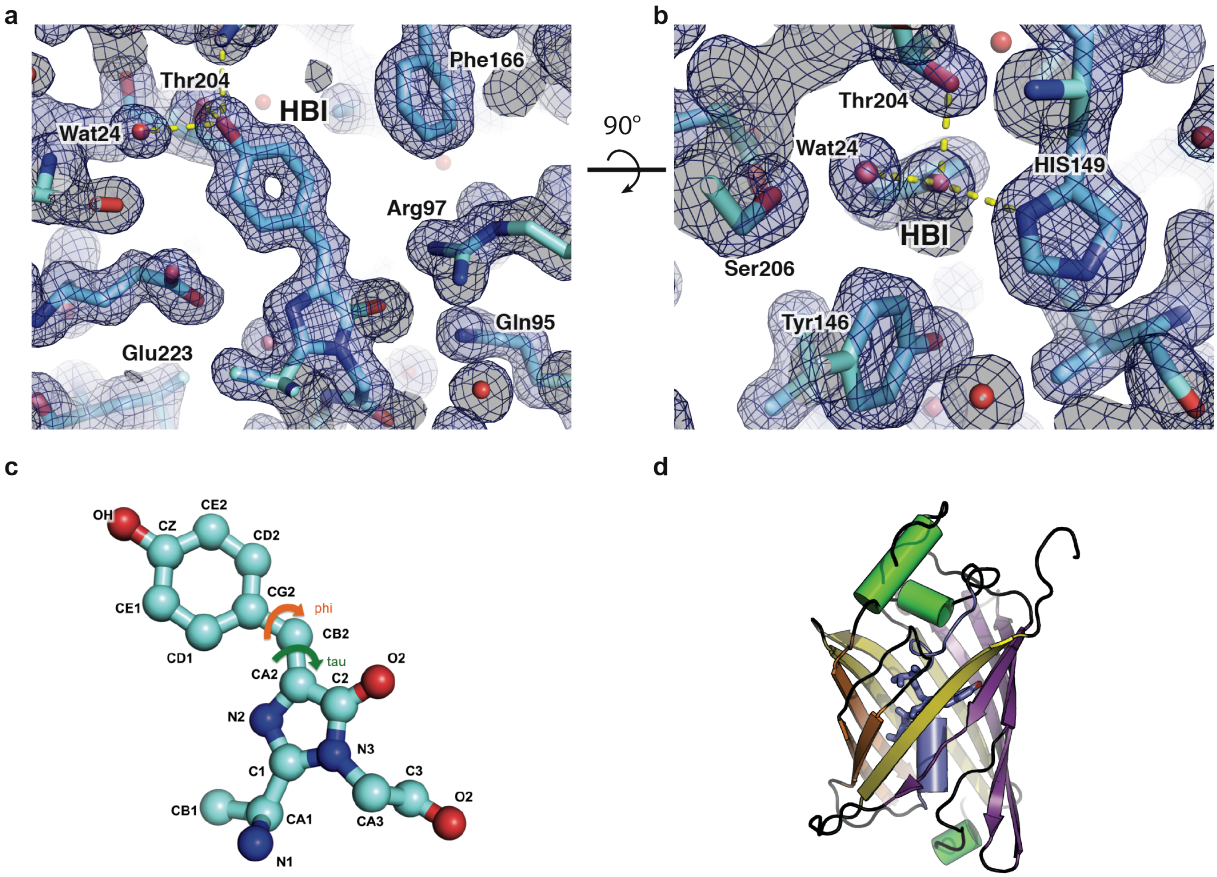

Supplementary Figure 16: SFX structure of rsEGFP2 in the *on* state. The final *on* model (cyan) is shown with a $2mF_{obs}^{reference} - DF_{calc}$ map contoured at 1 σ. Panels (*a*) and (*b*) show two views, 90° apart. In panel (*b*), the H-bonding partners of the chromophore (HBI) phenol group are shown, namely His149, Thr204 and Wat24 (H-bond lengths of 2.9, 2.8 and 2.6 Å, respectively). (*c*) Topology of the chromophore in the *cis* isomer. Two dihedral angles (*tau* (C2-CA2-CB2-CG2) and *phi* (CA2-CB2-CG2-CD2)) determine the isomerization state of the chromophore (green and orange arrows, respectively). (*d*) Ribbon diagram of rsEGFP2. Strands whose residues face the chromophore phenol and imidazolinone groups are highlighted in purple and yellow, respectively. Strands whose residues face the α-helix N-terminal to the chromophore are highlighted in orange. The structural element holding the chromophore in the middle of the β-barrel, including the α-helix N-terminal to it, is shown in blue. Other α-helices are shown in green, and residues in loops are shown in black.

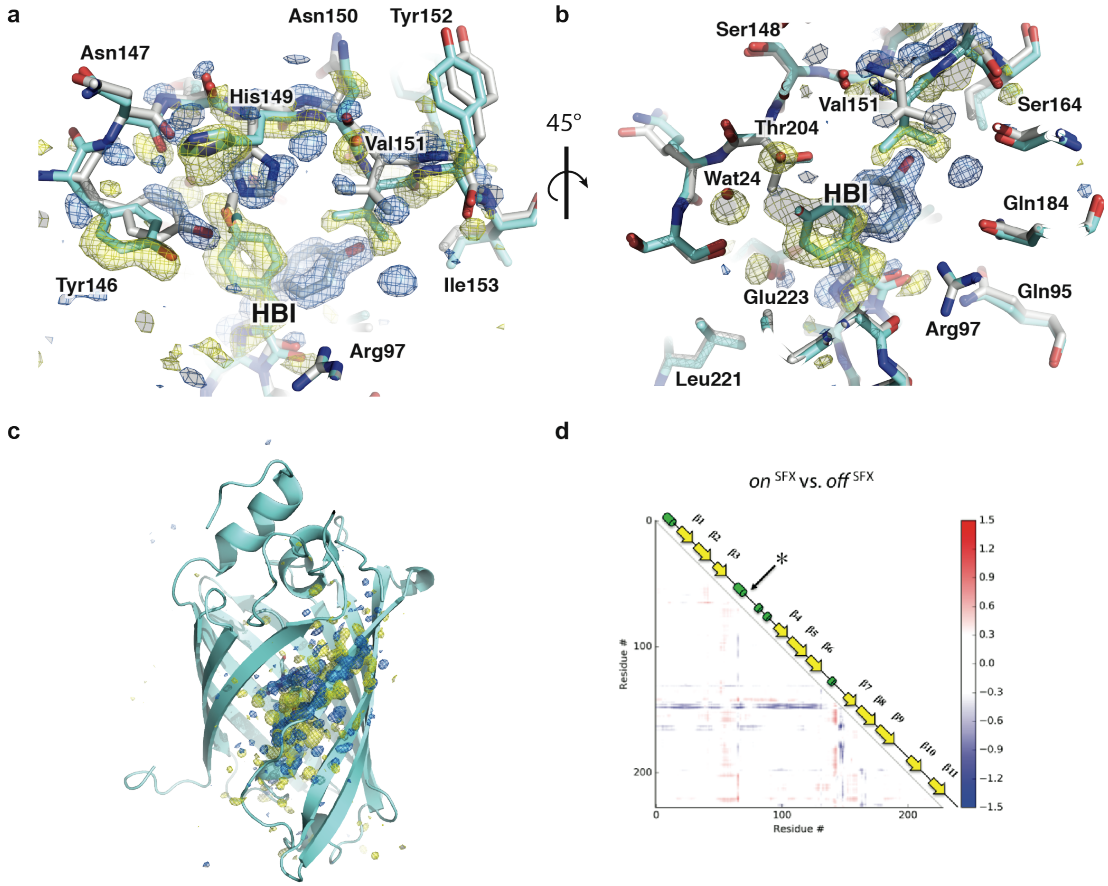

Supplementary Figure 17 : In-line pre-illumination of crystals results in efficient *on*-to-*off* transition. Q-weighted[54] difference Fourier map calculated between the reference (no pre-illumination) and the laser-off (pre-illumination at 488 nm) datasets, using the final *on* model for phasing. In all panels, the *on*-state model appears as a cyan carbon trace, and the *off*-state model as a grey carbon trace. Difference Fourier maps are contoured at ± 4.0 σ, with negative and positive peaks displayed in yellow and blue, respectively. Panels (*a*) and (*b*) show two views of the chromophore pocket, ~45° apart, and allow observing all conformational changes that accompany the *on*-to-*off* transition. This transition involves large conformational changes in residues from β-strand-7 (Tyr146, His149, Val151; mostly visible on panel (*a*)) and β-strand-10 (Thr204; mostly visible on panel (*b*)). These changes include both main and side chain atoms. (*c*) Overview of $F_{obs}^{laser\text{-}off}$-$F_{obs}^{reference}$ map. The ribbon diagram of the *on* model is shown in the same color as above. Only the chromophore is shown as sticks. (*d*) Distance difference matrix (DDM) calculated between structures of rsEGFP2 from SFX *on*- and laser-off structures. The position of the chromophore is indicated by *. The *on*-state structure appears more compact than the laser-off structure. Residues in β-strand-7 (*i.e.* residues 149 to 156) show the largest backbone deviation, moving closer to the chromophore in the *on*-state structure.

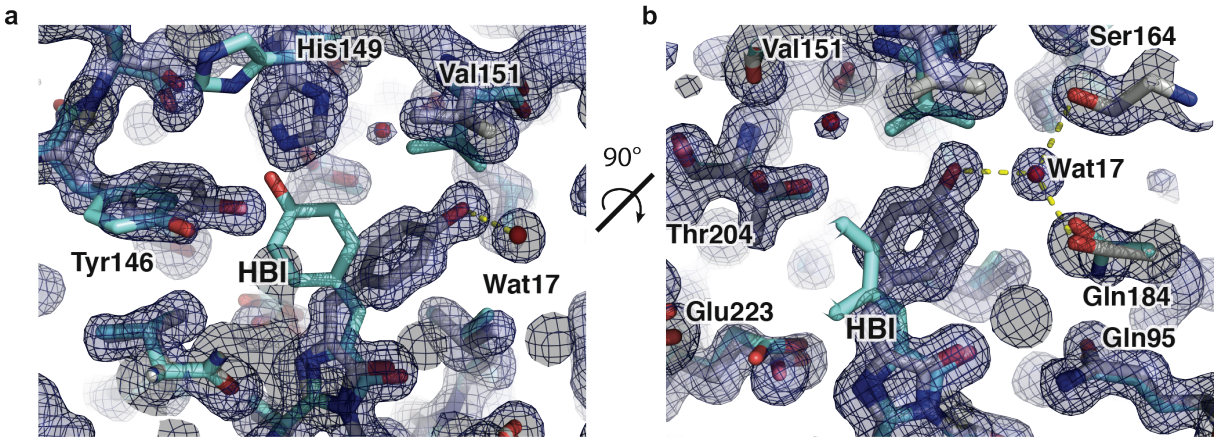

Supplementary Figure 18: Occupancy of the *on*-state conformer in the laser-off dataset. In both panels, the *off*-state conformer of the laser-off structure appears as a grey carbon trace, and its *on*-state conformer as a cyan carbon trace. (*a*, *b*) $2mF_{obs}^{\text{laser-off}}$ - DF_{calc} map calculated from the laser-off dataset. Views (*a*) and (*b*) are roughly 90° apart. In panel (*b*), Wat17 is shown, which is H-bonded to the phenol hydroxyl group of the *off*-state chromophore (distance: 2.7 Å). This water is also H-bonded to Ser164 and Gln184 (2.9 and 2.9 Å distance, respectively).

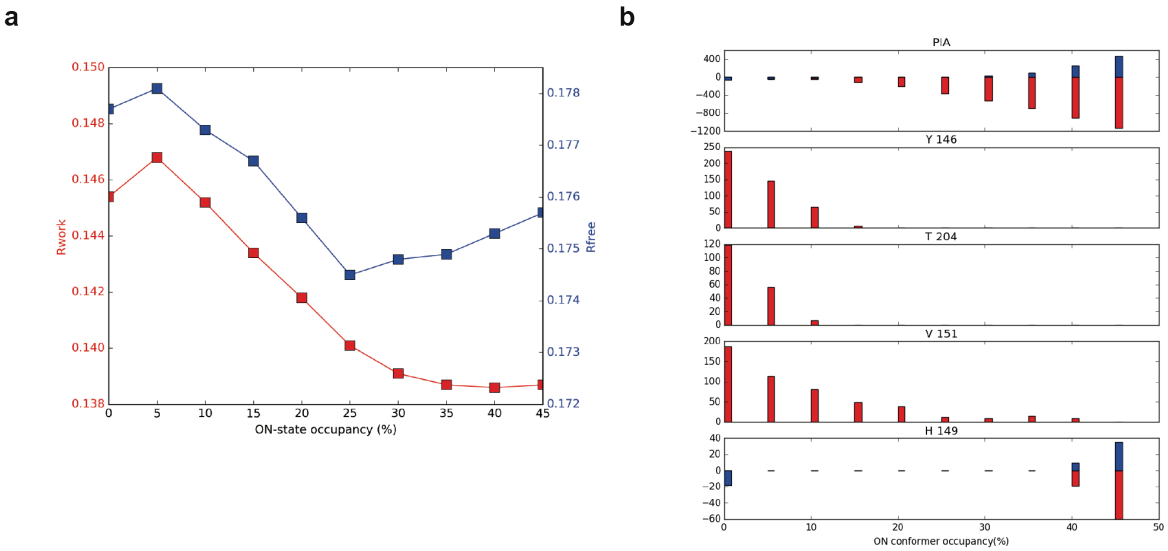

Supplementary Figure 19: Occupancy of the *on*-state conformer in the laser-off dataset (*a*). R_{free} (blue) and R_{work} (red) values obtained when refining the laser-off dataset with 0 to 45% of the *on*-state model and 100 to 55% of the *off* model. The plot suggests that the best model is that composed of 25 and 75% of *on*-state and *off*-state conformers. (*b*) Integration of positive and negative $mF_{obs}^{laser\text{-}off}$-$DF_{calc}$ peaks on key residues subject to structural rearrangements upon *off*-to-*on* transition. Peaks located on the *off*-state and *on*-state conformers are colored in blue and red, respectively. Strong negative peaks are observed on the *on*-state chromophore in $mF_{obs}^{laser\text{-}off}$-$DF_{calc}$ maps with an *on*-state occupancy higher than 10%. Therefore, we set the relative occupancy of the *on*-state and *off*–state conformers to 10 and 90%, respectively, in the final *laser-off* model.

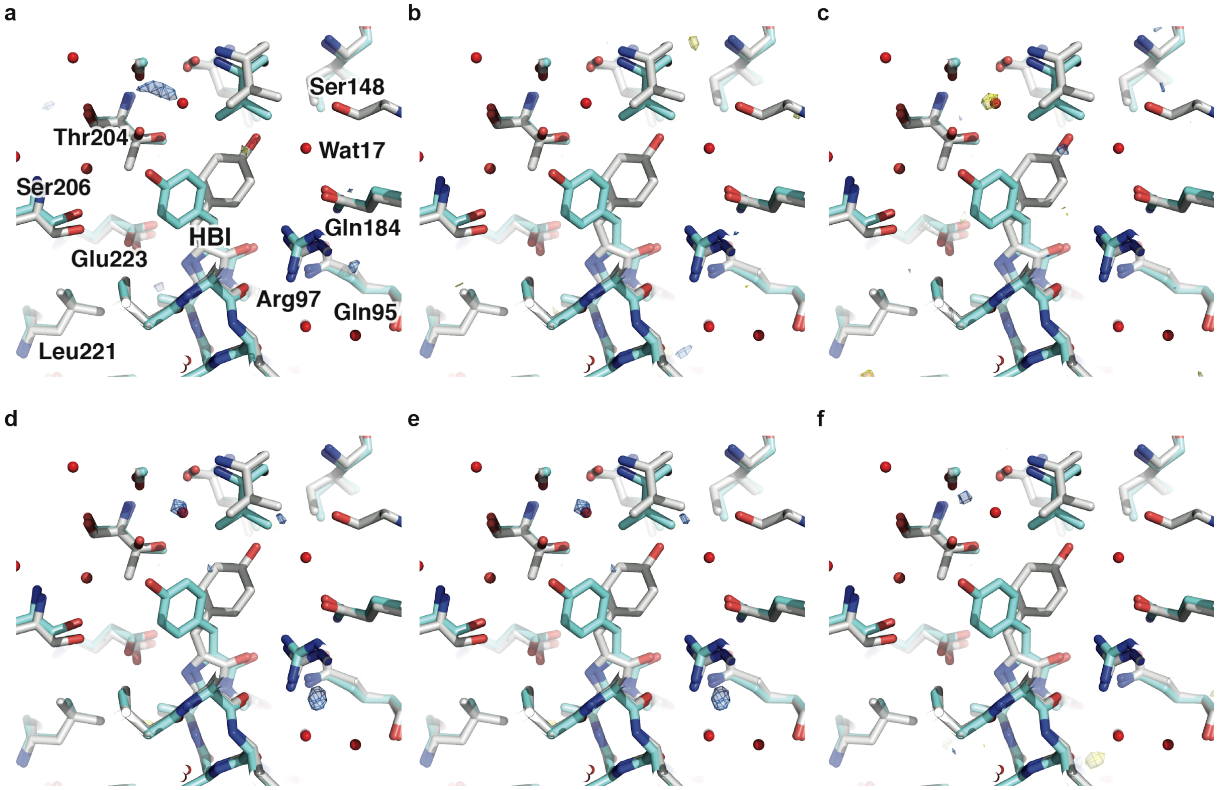

Supplementary Figure 20: All laser-off data collected over three experimental shifts contain similar structural information. Q-weighted[54] difference Fourier maps calculated from reduced laser-off datasets produced on a per-shift basis (1st row) or by a combination of shifts (2nd row). The complete laser-off dataset was used as a reference, and phases were calculated from the final laser-off model, consisting of 90% and 10% of *off*- and *on*-state conformers, respectively. In all panels, the *off*-state model appears as a grey carbon trace, and the on-state model as a cyan carbon trace. Difference Fourier maps are contoured at ± 3.5 σ, with negative and positive peaks displayed in yellow and blue, respectively. (*a*) 1st shift (12 hours); (*b*) 2nd shift; (*c*) 3rd shift; (*d*) 1st and 2nd shifts; (*e*) 1st and 3rd shifts; (*f*) 2nd and 3rd shifts. (*a-f*) Regardless of which reduced laser-off dataset is considered, the difference Fourier maps are virtually featureless, indicating that the structural information collected during the various shifts is both qualitatively and quantitatively highly similar. Thus, the pre-illumination setup and the *on*-to-*off* photoswitching efficiency were stable over the course of the three shifts. The flatness of these maps validates the merging of laser-off data collected during the three shifts.

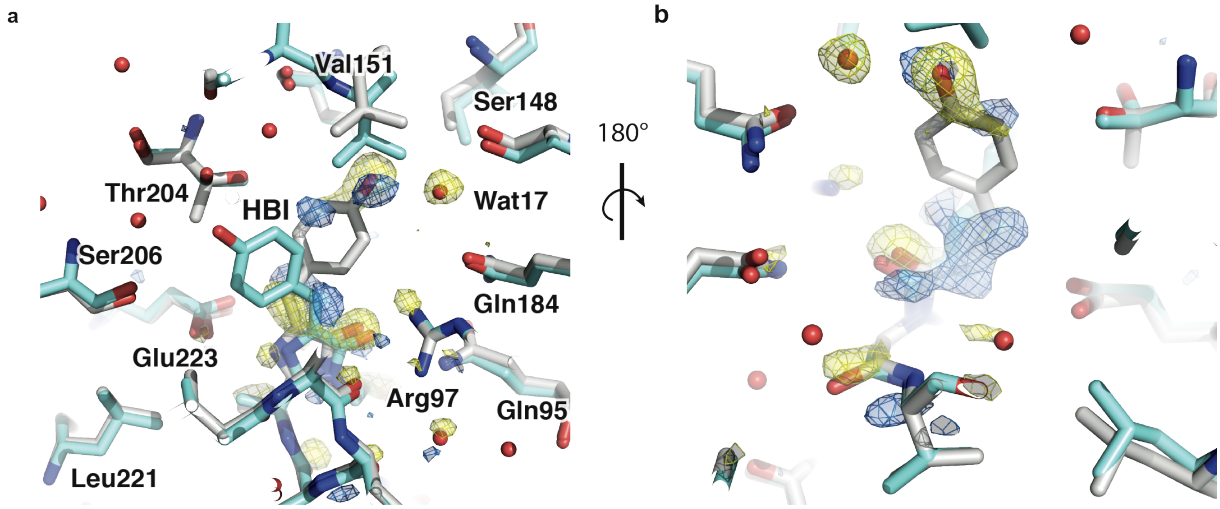

Supplementary Figure 21: Pump-laser illumination at 400 nm results in conformational changes in the chromophore region after 1 ps. Q-weighted[54] difference Fourier map ($F_{obs}^{\text{laser-on-}\Delta 1ps}$-$F_{obs}^{\text{laser-off}}$) calculated between the laser-on-Δ1ps dataset and the laser-off dataset, using the final laser-off model consisting of 90% and 10% of *off*- and *on*-state conformers, respectively for phasing. The *off*-state model appears as a grey carbon trace, and the *on*-state model as a cyan carbon trace. Difference Fourier maps are contoured at $\pm$ 3.5 σ, with negative and positive peaks displayed in yellow and blue, respectively. Panels (*a*) and (*b*) show two views of the chromophore pocket, rotated by ~180°, allowing to observe peaks on both sides of the chromophore. Strong negative peaks, up to -10 σ, are seen on the phenol hydroxyl, imidazolinone carbonyl oxygen and methylene linker of the *off*-state chromophore, as well as on waters 8, 17, and 19 which are H-bonded to it. These negative peaks indicate that the fraction of crystalline *off*-state chromophore is decreased, 1 ps post-pumping at 400 nm, and that waters in direct interaction with the chromophore are affected at the same time. Negative peaks are also observed on side chain atoms of residues stabilizing the chromophore imidazolinone ring (Gln95, Arg97 and Glu223), and on backbone atoms of residues N-terminal or C-terminal to the chromophore (Leu61 to Cys71, where the chromophore is HBI). In addition, positive peaks are seen mid-way between the *on*- and *off*-state chromophore. Hence, a fraction of the crystalline *off* chromophore has transitioned to a new state. A positive peak is also seen for Wat17, suggesting that it accompanies this transition.

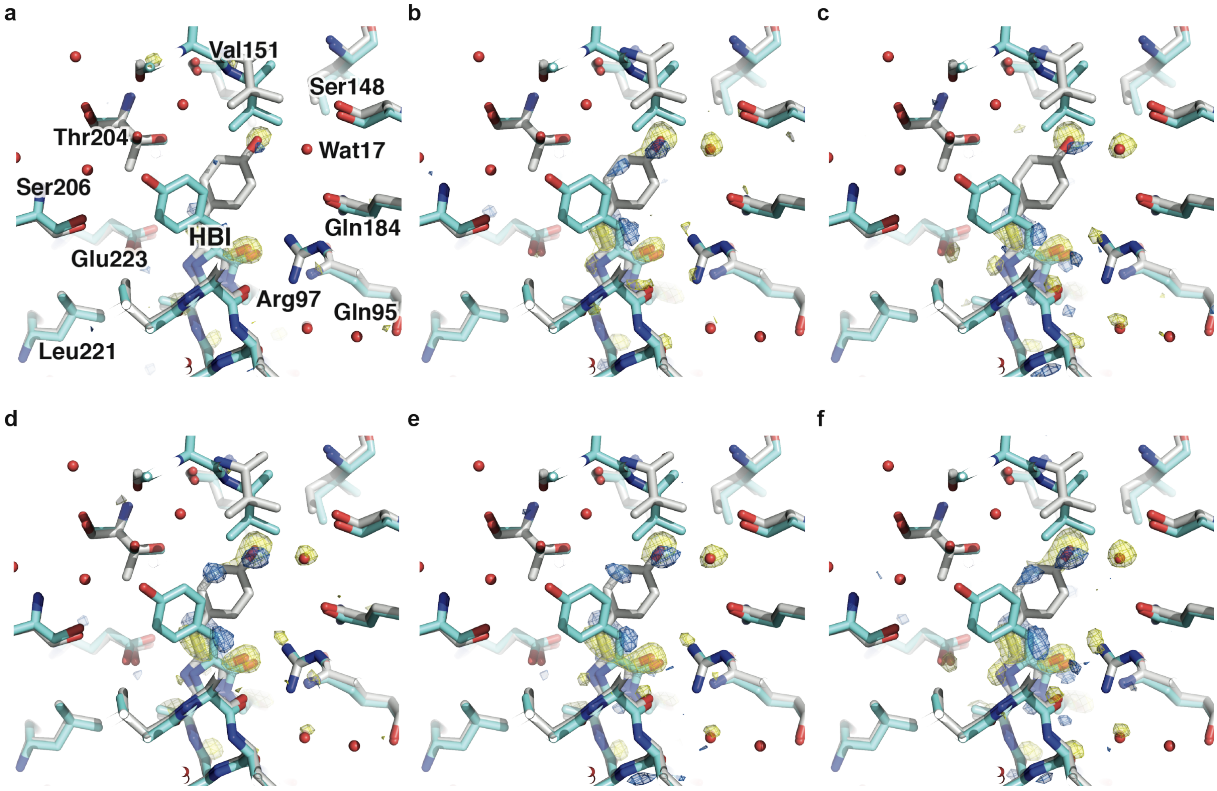

Supplementary Figure 22: All laser-on-Δ1ps data collected over three experimental shifts contain similar structural information. Q-weighted[54] difference Fourier maps calculated from segmented laser-on-Δ1ps datasets produced on a per-shift basis (1st row) or by binary combination of shifts (2nd row). The final laser-off dataset was used as a reference, and phases were calculated from the final laser-off model, consisting of 90 and 10% of *off*- and *on*-state conformers, respectively. In all panels, the *off*-state model appears as a grey carbon trace, and the *on*-state model as a cyan carbon trace. Difference Fourier maps are contoured at $\pm$ 3.5 σ, with negative and positive peaks displayed in yellow and blue, respectively. (*a*) 1st shift (12 hours); (*b*) 2nd shift; (*c*) 3rd shift; (*d*) 1st and 2nd shifts; (*e*) 1st and 3rd shifts; (*f*) 2nd and 3rd shifts. (*a-f*) Regardless of which subset of the full laser-on-Δ1ps dataset is considered, the negative features of the maps are comparable, *i.e.* peaks of similar intensities are seen on the phenol hydroxyl, imidazolinone carbonyl oxygen and methylene linker of the chromophore, as well as on waters 8, 17, and 19. As for positive peaks, these only rise above 3.5 σ in difference Fourier maps calculated from data combination from two shifts, illustrating the direct relationship between the clearness of map features and the number of indexed patterns used to produce parent datasets. More importantly, the similarity between the difference Fourier maps shown in panels *a-f* and that computed from the complete laser-on-Δ1ps dataset (shown in Supplementary Fig. 20) retrospectively validates the merging of laser-on-Δ1ps data collected over the three shifts.

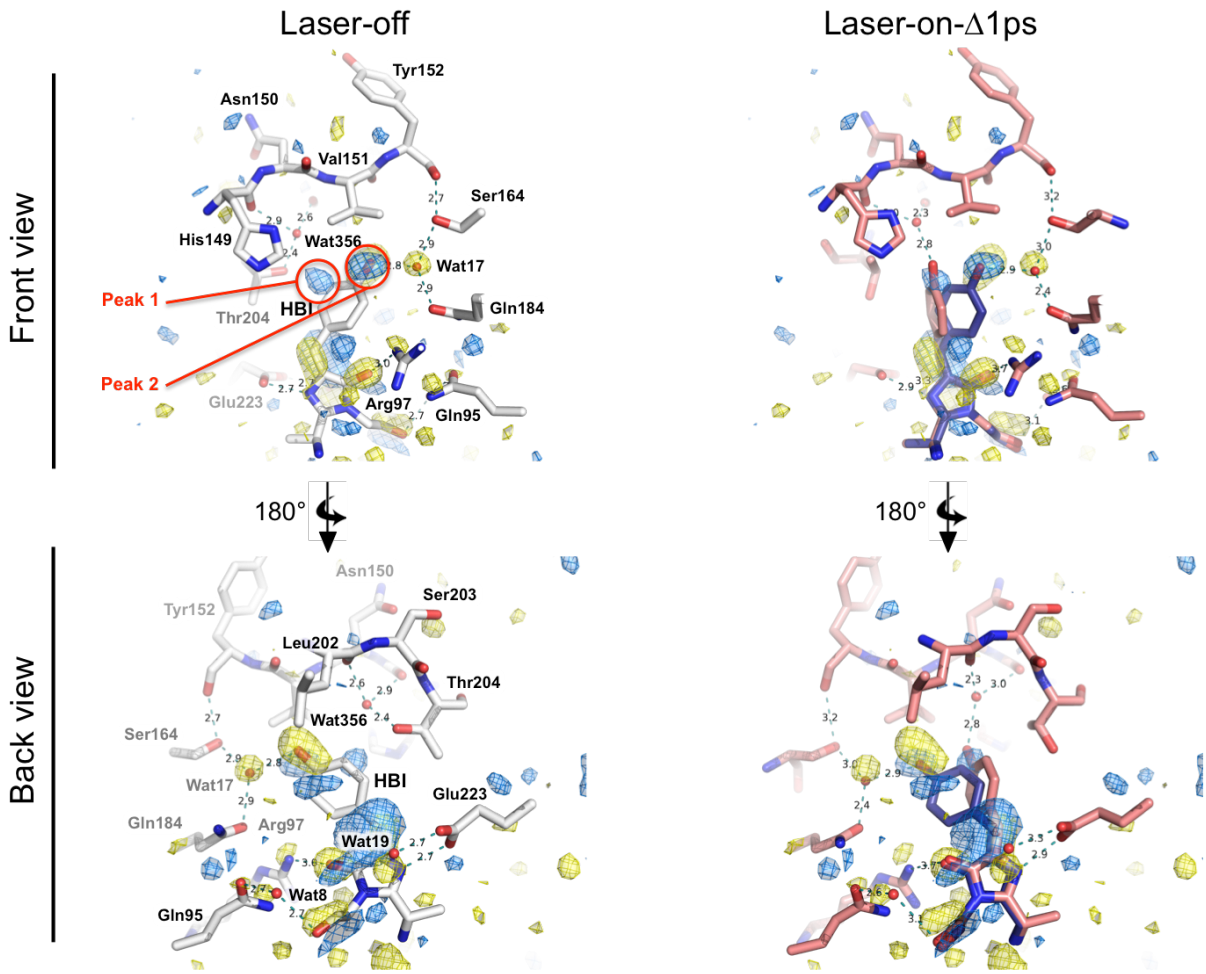

Supplementary Figure 23: Peaks in the Q-weighted[54] $F_{obs}^{\text{laser-on-}\Delta 1ps}$-$F_{obs}^{\text{laser-off}}$ map are concentrated around the chromophore region. Upper and lower panels show opposite views of the chromophore region. The *off*-state model (grey) accounting for 90% of the laser-off data set is displayed in the left panels, and the difference-refined laser-on-Δ1ps model is shown in the right panels (model T in pink, and model P in blue). In all panels, the $F_{obs}^{\text{laser-on-}\Delta 1ps}$-$F_{obs}^{\text{laser-off}}$ map is contoured at ± 3σ. Red circles highlight peaks 1 and 2 into which model T and model P were built, respectively. Residues visible in the panels are those that display peaks higher than ± 3σ in the vicinity of the chromophore, and they accordingly display dynamics in the difference-refined structure (right panels). Structural waters interacting with the chromophore are also shown. Hydrogen-bonds are highlighted by dashed lines, and the bond-length (in Å) overlaid on these. Wat17 and Wat356 are obligate acceptors in the H-bond they establish with the chromophore, implying that the phenol OH of the chromophore can only interact with one of them at the time. H-bonding to Wat17 is thus exclusive to the *off*-state chromophore and to model P, while H-bonding to Wat356 is the preserve of model T. Formation of model T is accompanied by a 120° rotation in the side chain of Thr204, hitherto H-bonded in a similar fashion (obligate donor) to Wat356.

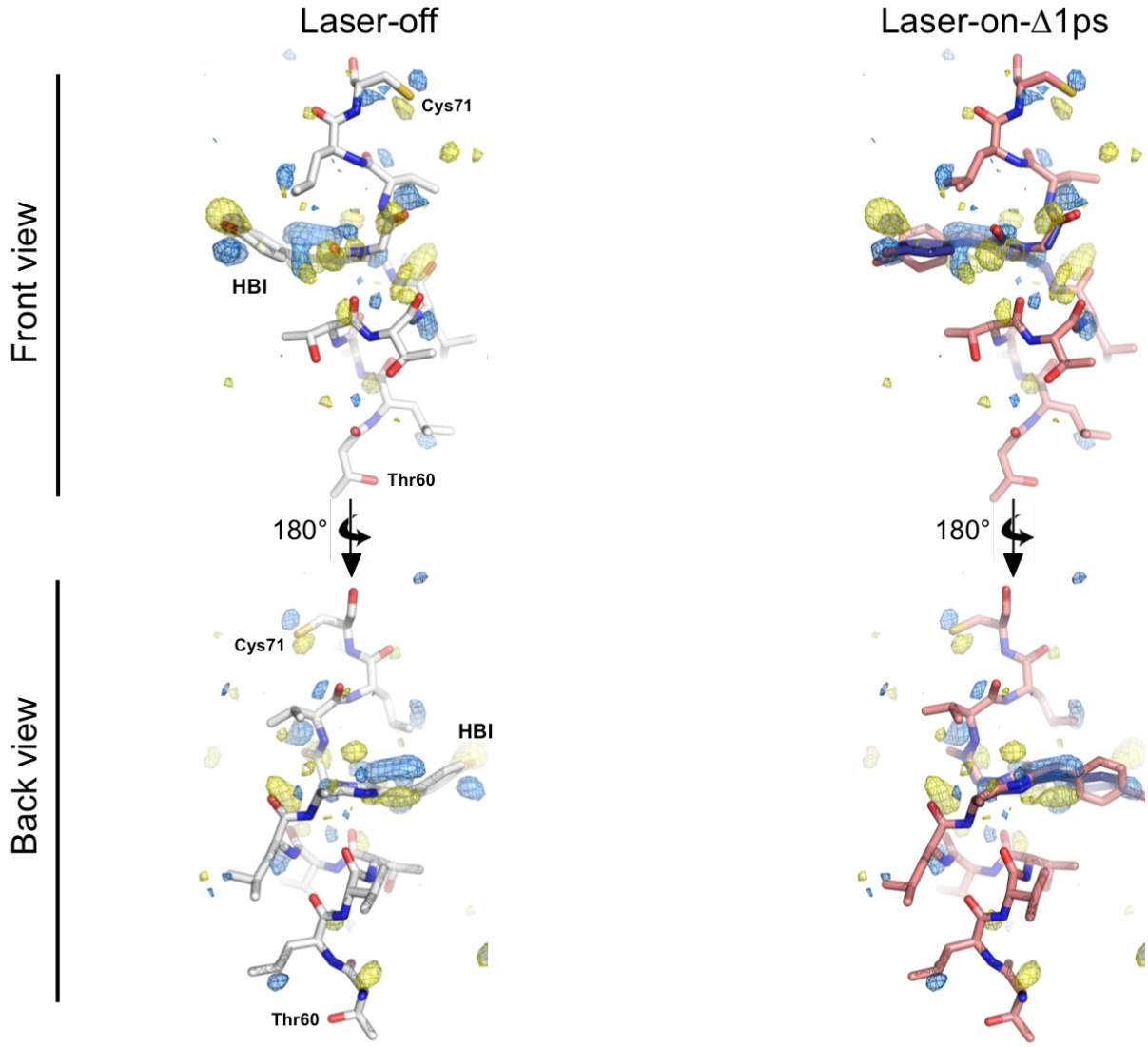

Supplementary Figure 24: The α-helix N-terminal to the chromophore features a succession of peaks in the Q-weighted[54] $F_{obs}^{\text{laser-on-}\Delta 1ps}$-$F_{obs}^{\text{laser-off}}$ map. Upper and lower panels show opposite views of the α-helix N-terminal to the chromophore. The *off*-state model accounting for 90% of the laser-off data set is displayed in the left panels (grey), and the difference-refined laser-on-Δ1ps model is shown in the right panels (model T in pink, and model P in blue). In all panels, the $F_{obs}^{\text{laser-on-}\Delta 1ps}$-$F_{obs}^{\text{laser-off}}$ map is contoured at ± 3σ. All residues in the α-helix N-terminal to the chromophore show peaks in the difference map and likewise for the three residues C-terminal to it.

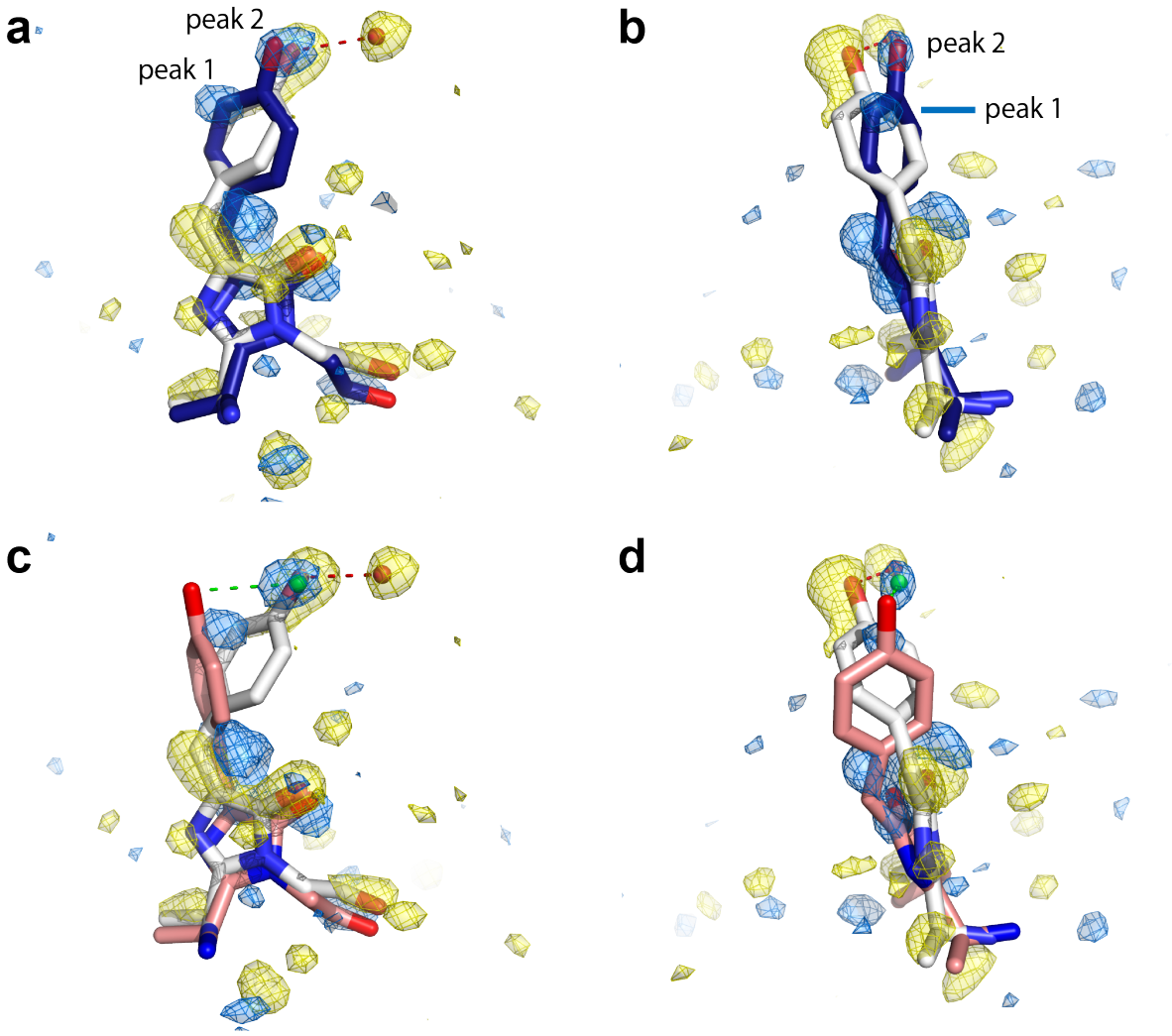

Supplementary Figure 25: Modeling of the *intermediate* state models at 1 ps. In all panels (*a-d*), the Q-weighted[54] difference Fourier map ($F_{obs}^{\text{laser-on-}\Delta 1ps}$-$F_{obs}^{\text{laser-off}}$) calculated between the laser-on-Δ1ps dataset and the laser-off dataset, is contoured at $\pm$ 3.5 σ , with negative and positive peaks displayed in yellow and blue, respectively. The *off*-state model appears as a grey carbon trace, and the *intermediate*-state models P (*a, b*) and T (*c, d*) are shown as blue and pink carbon traces, respectively. Negative peaks are observed on the *off*-state chromophore, suggesting that upon pumping at 400 nm and at a pump-probe delay of 1ps, the latter has been depleted. Two positive peaks appear midway between the *on* (not shown; see Supplementary Fig. 21 and 22) and *off*-state conformations of the chromophore, suggesting the buildup of an intermediate state: two conformations of the chromophore could explain these two peaks. (*a, b*) In model P, the chromophore OH and CE1 fit in the two peaks. However, the large bilobal peak observed on the imidazolinone is only partially accounted for. (*c, d*) In model T, the chromophore OH fits in peak 1, whereas peak 2 accommodates water 17, H-bonded to the chromophore OH in the *off*-state conformation. This model provides a better fit for the peak observed on the imidazolinone but implies that the H-bond between the chromophore OH and water 17 is preserved after the transition to the intermediate state.

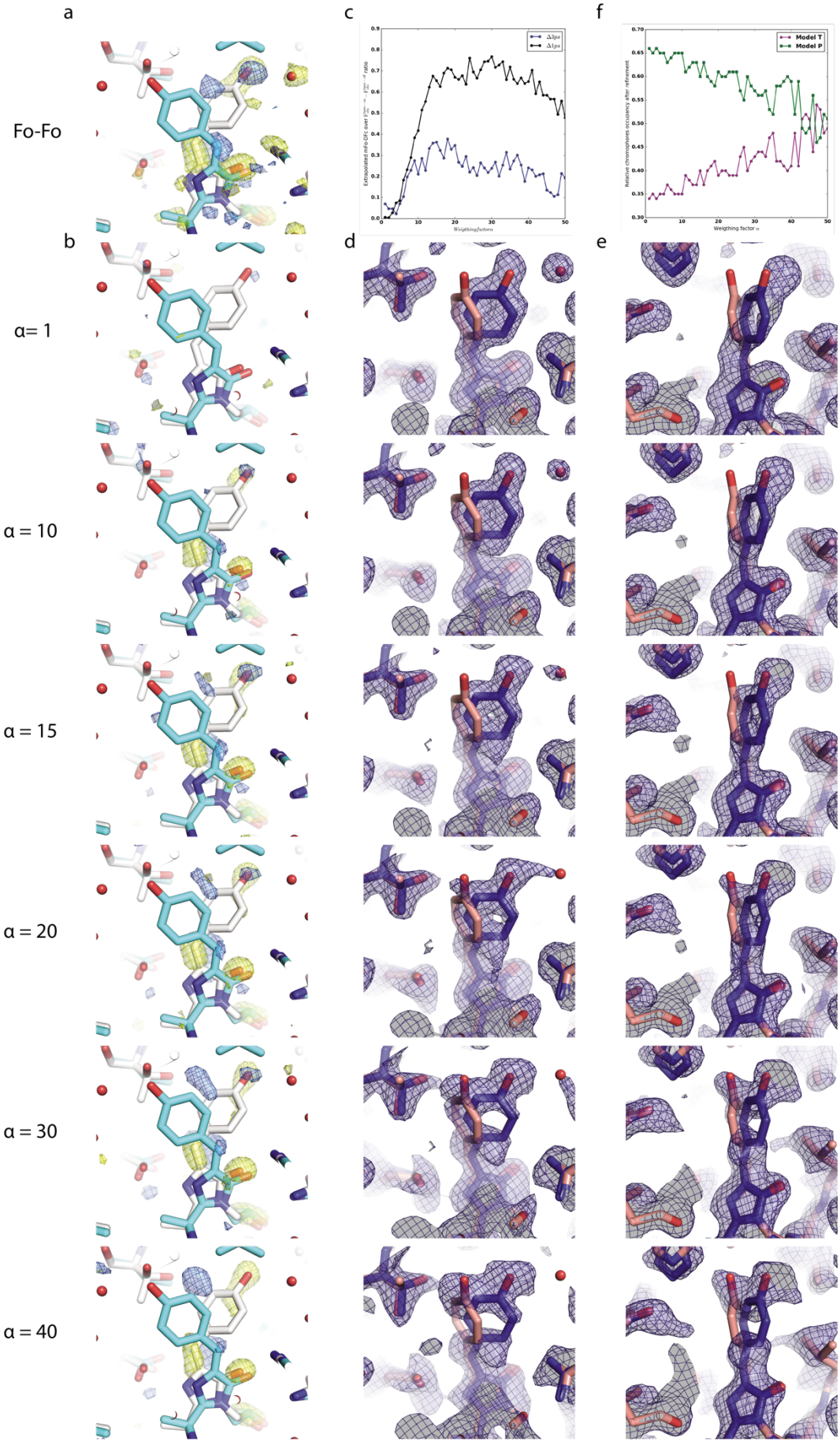
a
b
c
d
e
f
Fo-Fo
α= 1
α = 10
α = 15
α = 20
α = 30
α = 40
Model T
Model P
Weighting factor ω

Supplementary Figure 26: **Determination of absolute and relative occupancy of models T and P at 1 ps.** (*a*) Experimental $F_{obs}^{\text{laser-on-}\Delta 1ps}$ - $F_{obs}^{\text{laser-off}}$ map contoured at 3σ. The laser-off model is displayed, with the chromophore *off*- and *on*-conformers represented as white and cyan sticks, respectively. (*b*) $F_{extrapolated}^{\text{laser-on-}\Delta 1ps}$ - $F_{calc}^{\text{laser-off}}$ maps obtained from extrapolated structure factors calculated using increasing α values and phased using the laser-*off* model. All maps are contoured at ± 3σ. At α=1, which would correspond to 100% occupancy of the intermediate state, the $F_{extrapolated}^{\text{laser-on-}\Delta 1ps}$ - $F_{calc}^{\text{laser-off}}$ map is featureless. When α reaches 15, the resulting $F_{extrapolated}^{\text{laser-on-}\Delta 1ps}$ - $F_{calc}^{\text{laser-off}}$ map reveals peaks qualitatively and quantitatively similar to those observed in the experimental $F_{obs}^{\text{laser-on-}\Delta 1ps}$ - $F_{obs}^{\text{laser-off}}$ map. (*c*) Determination of α, *i.e.* the inverse of the intermediate state occupancy. $F_{extrapolated}^{\text{laser-on-}\Delta 1ps}$ - $F_{calc}^{\text{laser-off}}$ peaks higher than ± 3σ (b) observed in a radius of 1.5 Å around the chromophore atoms in all its conformations (*off* and *on* conformers, as well as models T and P) were integrated and the ratio of their absolute sum over the overall signal of the experimental $F_{obs}^{\text{laser-on-}\Delta 1ps}$ - $F_{obs}^{\text{laser-off}}$ (black) was plotted. We attempted to use the same approach to determine α for the laser-on-Δ3ps (blue). For the laser-on-Δ1ps dataset, this ratio increases with α values up to ~15, and then reaches a plateau at ~0.8. For the laser-on-Δ3ps dataset, the curve shape is similar but the plateau only reaches 0.3. Therefore, we decided not to perform difference refinement with the laser-on-Δ3ps dataset. (*d, e*) $2mF_{extrapolated}^{\text{laser-on-}\Delta 1ps}$ - $DF_{calc}^{\text{laser-off}}$ maps obtained from extrapolated structure factors calculated using increasing α values, and phased using the laser-*off* model. All maps are contoured at 1σ. The chromophore models T and P are shown in salmon and blue sticks, respectively (*d*, *e*). α values are identical to those used to generate the $F_{extrapolated}^{\text{laser-on-}\Delta 1ps}$ - $F_{calc}^{\text{laser-off}}$ maps shown in (*b*). For α=1, the density is surrounding the *off*-state chromophore (model not shown), but with increasing α values, electron density builds up around model T and model P. Recall that no phase information from the latter was introduced during map computation. (*f*) Refined occupancies of model T (magenta) and model P (green) obtained at increasing α values in the laser-on-Δ1ps dataset.

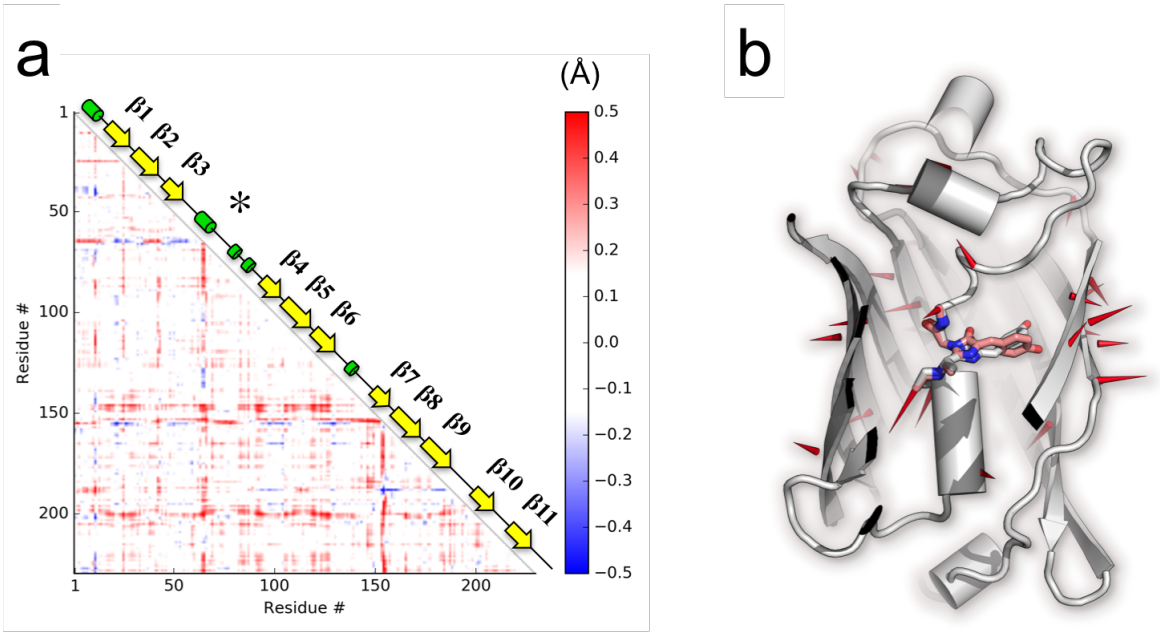

Supplementary Figure 27: The β-barrel expands upon the transition from the *off* state to model T. (*a*) Difference distance matrix calculated between the *off*-state structure and the difference-refined laser-on-Δ1ps structure. Red and blue indicate increasing and decreasing distances, respectively, in model T with respect to the *off*-state structure. (*b*) Porcupine plot of the differences between the *off*-state structure and the difference-refined laser-on-Δ1ps structure. The *off*-state (cyan) and model T (pink) chromophores are shown. The movement of Cα atoms by more than 0.2 Å is indicated by arrows on the ribbon representation, with the magnitude of motions illustrated by the length of arrows exaggerated seven fold to increase visibility.

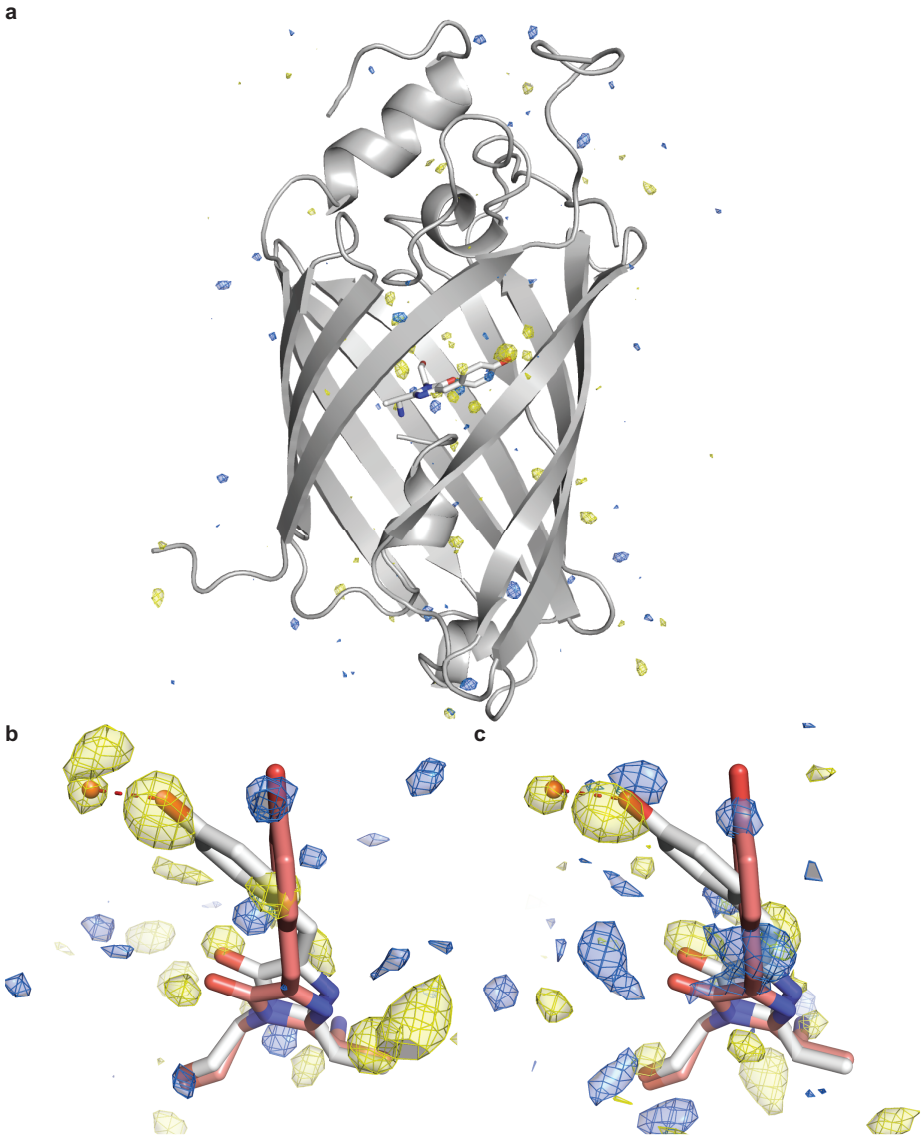

Supplementary Figure 28: After pumping at 400 nm, the crystalline system further evolves between 1 ps and 3 ps. (*a*) Overview of the Q-weighted[54] difference Fourier map ($F_{obs}^{\text{laser-on-}\Delta 3ps}$-$F_{obs}^{\text{laser-off}}$; contoured at $\pm$ 3.5 σ and colored as in Supplementary Fig. 23), overlaid on the *off*-state model (grey). (*b*, *c*) Close-up view of the *off*-state (grey) and *intermediate* chromophore model T (pink), overlaid with the $F_{obs}^{\text{laser-on-}\Delta 3ps}$-$F_{obs}^{\text{laser-off}}$ (*b*) and $F_{obs}^{\text{laser-on-}\Delta 1ps\text{-random}}$-$F_{obs}^{\text{laser-off}}$ (*c*) maps, both contoured at $\pm$ 3 σ . Comparison of (*b*) and (*c*) suggests that the *intermediate* state corresponding to model T has decayed on the 1 to 3 ps timescale.

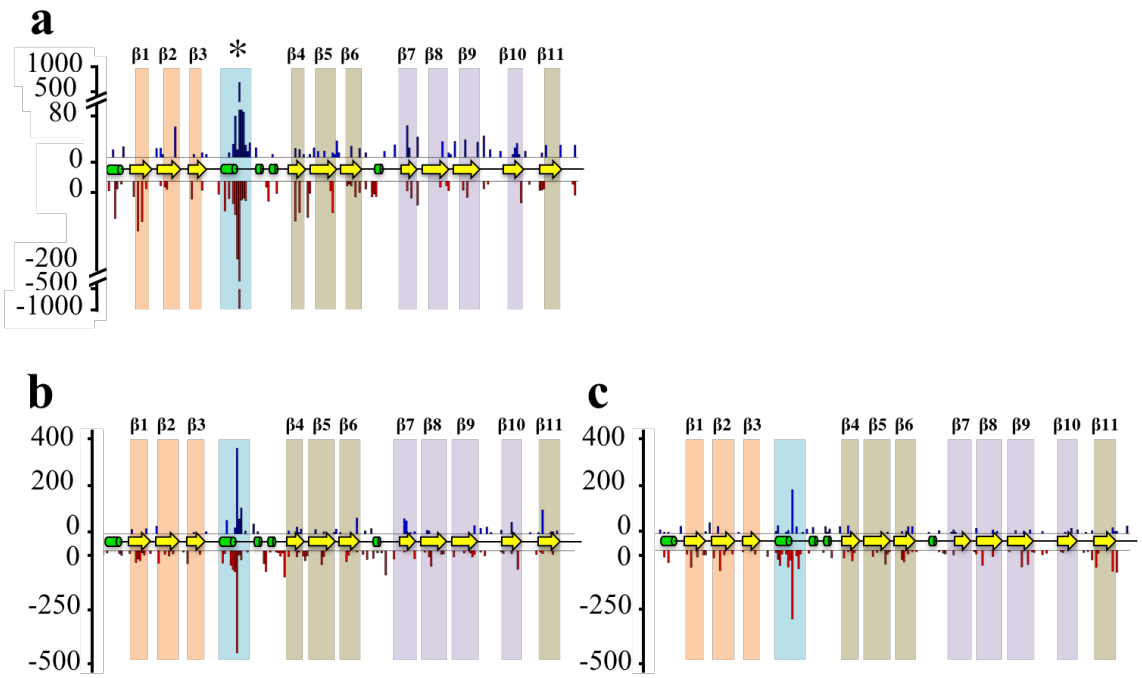

Supplementary Figure 29: Sequence-wise integration of peaks from Q-weighted[54] difference Fourier map $F_{obs}^{\text{laser-on-Δ1ps}}$-$F_{obs}^{\text{laser-off}}$ (*a*), $F_{obs}^{\text{laser-on-Δ1ps-random}}$-$F_{obs}^{\text{laser-off}}$ (*b*), and $F_{obs}^{\text{laser-on-Δ3ps}}$-$F_{obs}^{\text{laser-off}}$ (*c*). In all three panels, the x-axis corresponds to the protein sequence, with the secondary structure illustrated by a cartoon. The y-axis reports the integrated values of difference Fourier map peaks, with negative and positive peaks colored in red and blue, respectively. The α-helix central to the β-barrel and which supports the chromophore is highlighted by a blue shaded band. β-strands whose residues face the phenol and imidazolinone groups of the chromophore are highlighted by purple and yellow shaded bands, respectively. β-strands whose residues face the α-helix N-terminal to the chromophore are highlighted by orange shaded bands. All peaks higher than $\pm 3\sigma$ were integrated and assigned to the closest residue within a 1.5 Å radius. In panel (*a*), * indicates the peak corresponding to the chromophore. (*b, c*) For the sake of comparison, a laser-on-Δ1ps-random dataset was generated (with as many indexed images as in the laser-on-Δ3ps dataset). The integrated peak values for the chromophore, negative and positive alike, are decreased in the difference Fourier map calculated with the laser-on-Δ3ps dataset. Thus, the combined occupancy of model T and model P decreases on the 1-3 ps timescale, whereas the *off*-state chromophore appears to repopulate.

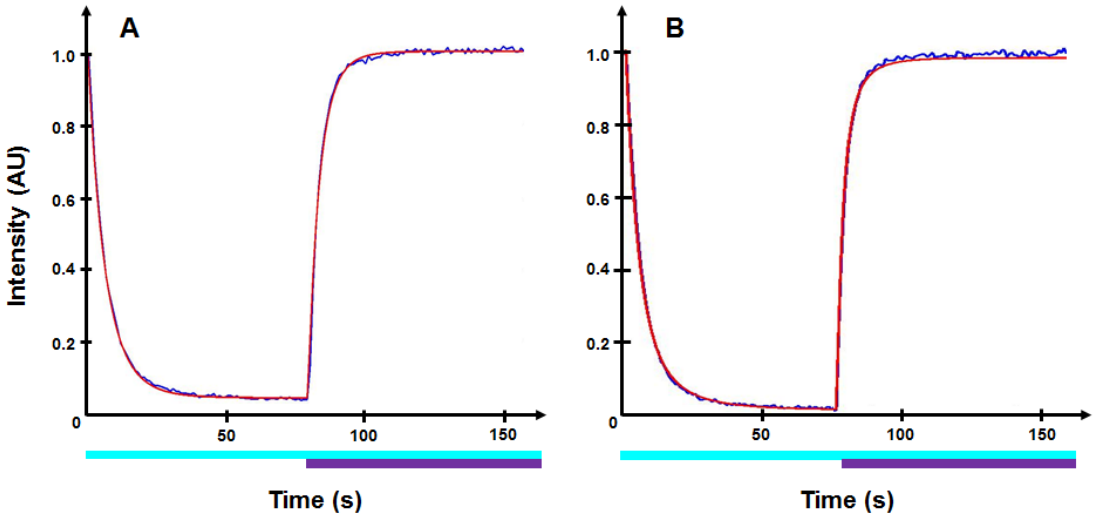

Supplementary Figure 30: Reversible switching cycle of rsEGFP2 (*a*) and rsEGFP2-V151A (*b*). Raw data (blue) were fitted (red) using a kinetic model involving one-to-one reversible conversion between the *on*- and the *off*-state. Cyan and violet lines represent the illumination times at 488- and 405-nm, respectively.

Supplementary Table 1 : Equilibrium bond lengths (Å) used in the excited-state MD simulations. All other values were taken from standard residues in the Amber force field. Atom names are according to Supplementary Fig. 16c.

	S_0	S_1
C1-N2	1.296	1.302
N2-CA2	1.410	1.359
CA2-CB2	1.367	1.419
CB2-CG2	1.445	1.399
CA2-C2	1.486	1.462
C2-O2	1.225	1.211
C2-N3	1.406	1.403
N3-C1	1.394	1.356
N3-CA3	1.458	1.448
C1-CA1	1.508	1.506

Supplementary Table 2 : Equilibrium angles (°). All other values were taken from standard residues in the Amber force field. Atom names are according to Supplementary Fig. 16c.

	S_0	S_1
C1-N2-CA2	107	108
N2-CA2-C2	108	108
CA2-C2-N3	103	103
C2-N3-C1	108	108
N3-C1-N2	114	112
N2-CA2-CB2	119	118
C2-CA2-CB2	133	134
CA2-CB2-CG2	134	132
CB2-CG2-CD1/CD2	120	120
N3-C2-O2	123	122
CA2-C2-O2	134	135

Supplementary Table 3 : Atomic charges (in a.u.). Atom names are according to Supplementary Fig. 16c.

	S_0	S_1
N1	-0.4157	-0.4157
H1	0.2719	0.2719
CA1	0.0236	0.0018
HA1	0.1301	0.1407
CB1	-0.1712	-0.1841
HB1 (3 atoms)	0.0395	0.0720
C1	0.5929	0.1047
N2	-0.6255	-0.4626
CA2	0.0691	0.3487
CB2	-0.1160	-0.4775
HB2	0.1605	0.1832
CG2	0.0484	0.2545
CD1 / CD2	-0.1139	-0.1480
HD1 /HD2	0.1570	0.1651
CE1 (CE2)	-0.3213	-0.3385
HE1 (HE2)	0.1875	0.1922
CZ	0.4182	0.4685
OH	-0.5536	-0.5457

HH	0.4007	0.3971
C2	0.5082	0.3331
O2	-0.4743	-0.5098
N3	-0.3261	-0.0604
CA3	-0.1529	-0.0370
HA3 (2 atoms)	0.1226	0.1009
C3	0.5973	0.5973
O3	-0.5679	-0.5679

Supplementary Table 4: Fluctuations (°) of the imidazolinone dihedral and improper angles during dynamics of the S_0 methyl-terminated anionic chromophore, obtained either by DFT/MD or by classical dynamics with the force field used in this work. Force constants k used in this work (kcal/mol for intra-cycle dihedrals, kcal/mol/radian^2 for improper dihedrals).

angle	Fluctuations		Force constants
	DFT/MD	Force field	*k*
Intra-cycle dihedrals			
C1-N2-CA2-C2	4.5	4.4	12.0
N2-CA2-C2-N3	5.6	5.0	5.5
CA2-C2-N3-C1	5.5	4.9	5.5
C2-N3-C1-N2	5.0	4.7	8.0
N3-C1-N2-CA2	3.8	4.0	16.0
Improper torsions			
CA2	7.3	6.9	6.0
C2	4.4	4.4	30.0
N3	15.1	11.9	4.0
C1	7.9	7.7	10.0

Supplementary Table 5: Data collection and refinement statistics

Dataset	*on*-state reference	laser-off	laser-on-Δ1ps	laser-on-Δ3ps	laser-on-Δ1ps-random
Pre-illumination (488 nm)	no	yes	yes	yes	yes
Pump-laser excitation (400 nm)	no	no	yes	yes	yes
Nominal pump-probe delay	n/a	n/a	1 ps	3 ps	1 ps
Space group	$P2_12_12_1$	$P2_12_12_1$	$P2_12_12_1$	$P2_12_12_1$	$P2_12_12_1$
Unit cell parameters					
a (Å)	51.7 ± 0.1	51.5 ± 0.1	51.5 ± 0.1	51.5 ± 0.1	51.5 ± 0.1
b (Å)	62.3 ± 0.1	62.9 ± 0.1	62.9 ± 0.1	62.9 ± 0.1	62.9 ± 0.1
c (Å)	71.9 ± 0.1	71.8 ±0.1	71.8 ±0.1	71.8 ±0.1	71.8 ±0.1
Collected frames	986,178	3,531,773	3,531,773	822,721	n/a
Indexed frames	34,731	65,102	64,629	22,262	22,262
Indexed frames (after outlier rejections)	34,715	65,097	64,620	22,259	22,260
Observations	6,655,463	13,199,336	13,080,130	4,176,799	4,698,783
Resolution (Å)	17.3 – 1.7 (1.76 - 1.70)	17.8 – 1.7 (1.76 – 1.70)	17.8 – 1.7 (1.76 – 1.70)	17.4 – 1.7 (1.76 – 1.70)	17.3 – 1.7 (1.76 – 1.70)
Rsplit (%)	9.1 (59.1)	6.8 (34.0)	6.8 (32.1)	11.4 (64.2)	11.8 (56.9)
CC*	0.996 (0.870)	0.998(0.962)	0.998(0.958)	0.995 (0.883)	0.995 (0.892)
I / σ(I)	9.2 (2.2)	11.5 (2.9)	11.4 (3.0)	7.3 (2.2)	6.8 (1.9)
Completeness (%)	99.8 (98.7)	99.8 (100)	99.9 (100)	98.0 (73.2)	99.9 (100.0)
multiplicity	254 (9)	665 (35)	516 (34)	162 (4)	179 (8)
Riso (with respect to dark dataset)*	22.0	n.a	5.0	7.5	6.8
Refinement statistics					
Refinement strategy	Classical refinement	Classical refinement	Difference-refinement		
PDB ID	5O89	5O8A	5O8B(#)		
Resolution (Å)	1.7 (1.76-1.70)	1.7 (1.76-1.70)	1.9 (1.97-1.90)		
Number of reflections	25573 (2287)	25880 (2384)	18792 (1708)		
Rfree	0.195 (0.308)	0.184 (0..263)	0.293 (0.379)		
Rwork	0.167 (0.244)	0.146 (0.196)	0.275 (0.344)		
Number of protein atoms	1960	3802	1936		
Number of water atoms	315	329	312		
B-factor protein ($Å^2$)	25.15	20.8	27.2		
r.m.s.d. bond lengths (Å)	0.006	0.006	0.003		
r.m.s.d. angles (°)	0.97	0.85	0.51		

Ramachandran favored	98.7	96.5	96.4		
Ramachandran allowed	1.3	2.6	3.6		
Ramachadran outliers	0	0.9	0.0		
Rotamer outliers	0	0.48	0.45		
C-beta outliers	0	0	0		
Clashscore	3.63	6.81	6.49		

*R_{iso} was calculated using Scaleit[65]

#5O8B corresponds to the difference-refined excited-state structure of rsEGFP2 1 ps following 400 nm-laser irradiation of the *off* state and contains extrapolated structure factors defined by eq. 1 in the Supplementary section entitled '*1-ps intermediate-state structure: data collection, modeling and refinement'.* Also, a composite structure based on 5O8A and 5O8B (83% *off* state, 10% *on* state, 4% model P, 3% model T) and containing observed structure facture amplitudes $F_{obs}^{\text{laser-on-}\Delta 1\text{ps}}$ has been deposited under accession code 5O8C.

Supplementary Table 6 : Effect of various merging schemes on overall data statistics

Dataset	# indexed patterns	Overall Signal to noise ratio (Monte-Carlo and scaling)	Rsplit (%)				
			Monte-Carlo	Monte-Carlo and scaling	Monte-Carlo and partiality	Monte-Carlo Partiality Scaling	Monte-Carlo Partiality Scaling Post-refinement
reference	34731	9.2	10.8	9.1	11.4	9.9	9.8
laser-on-Δ1ps	64629	10.1	9.5	7.3	11.1	8.7	9.1
laser-off	65102	10.0	9.6	7.3	11.2	8.78	9.1
laser-on-Δ3ps	22262	7.3	13.4	11.4	14.5	12.9	12.6
Shift 3 – pump on	16333	5.5	16.4	14.1	18.0	15.6	15.8
Shift 3 – pump off	16415	5.5	16.3	14.0	17.7	15.4	16.3
Shift 4 – pump on	24072	6.5	14.5	11.4	15.8	13.2	13.1
Shift 4 – pump off	24260	6.5	14.5	11.5	15.7	13.1	13.0
Shift 5 – pump on	24224	7.1	13.5	11.1	14.6	12.6	12.3
Shift 5 – pump off	24427	7.1	13.2	10.9	14.5	12.6	12.4
Shifts 3 & 4 – pump on	40405	7.9	11.7	9.2	13.3	10.7	11.1
Shifts 3 & 4 – pump off	40675	8.0	11.7	9.2	13.2	10.7	11.1
Shifts 3 & 5 – pump on	40557	8.1	11.6	9.2	13.3	10.6	10.9
Shifts 3 & 5 – pump off	40842	8.1	11.8	9.3	13.4	10.7	11.1
Shifts 4 & 5 – pump on	48296	9.0	10.3	8.2	11.7	9.7	9.7
Shifts 4 & 5 – pump off	48687	9.0	10.4	8.2	11.8	9.7	9.9

Merging was performed at 1.6 Å resolution with 3 iterations when needed, and using the scsphere model for estimating partiality [66].

Supplementary Table 7 : Photophysical parameters of rsEGFP2 WT and rsEGFP2-V151A at pH 7.5

	rsEGFP2	rsEGFP2-V151A
Absorption maximum *on* [nm]	479	483
Absorption maximum *off* [nm]	406	404
On-to-*off* photoswitching quantum yield (Φ_{off})	0.04	0.06
Off-to-*on* photoswitching quantum yield (Φ_{on})	0.40	0.77
Extinction coefficient (ε) *on* [$M^{-1}.cm^{-1}$]	57 150	47 660
Extinction coefficient (ε) *off* [$M^{-1}.cm^{-1}$]	22 000	24 640

References

1. Colletier, J.P. et al. Serial Femtosecond Crystallography and Ultrafast Absorption Spectroscopy of the Photoswitchable Fluorescent Protein IrisFP. *J Phys Chem Lett* (2016).
2. Yadav, D. et al. Real-time monitoring of chromophore isomerization and deprotonation during the photoactivation of the fluorescent protein Dronpa. *J Phys Chem B* **119**, 2404-14 (2015).
3. Lincoln, C.N., Fitzpatrick, A.E. & van Thor, J.J. Photoisomerisation quantum yield and non-linear cross-sections with femtosecond excitation of the photoactive yellow protein. *Phys Chem Chem Phys* **14**, 15752-64 (2012).
4. Hutchison, C.D.M. et al. Photocycle populations with femtosecond excitation of crystalline photoactive yellow protein. *Chemical Physics Letters* **654**, 63-71 (2016).
5. Feliks, M. & Field, M.J. Pcetk: A pDynamo-based Toolkit for Protonation State Calculations in Proteins. *J Chem Inf Model* **55**, 2288-96 (2015).
6. Field, M.J. The pDynamo Program for Molecular Simulations using Hybrid Quantum Chemical and Molecular Mechanical Potentials. *J Chem Theory Comput* **4**, 1151-61 (2008).
7. Bashford, D. An Object-Oriented Programming Suite for Electrostatic Effects in Biological Molecules. *Lecture Notes in Computer Science* **1343**, 233-240 (1997).
8. Brooks, B.R. et al. CHARMM: A program for macromolecular energy, minimization, and dynamics calculations. *Journal of Computational Chemistry* **4**, 187-217 (1983).
9. Brooks, B.R. et al. CHARMM: the biomolecular simulation program. *J Comput Chem* **30**, 1545-614 (2009).
10. MacKerell, A.D. et al. All-atom empirical potential for molecular modeling and dynamics studies of proteins. *J Phys Chem B* **102**, 3586-616 (1998).
11. Reuter, N., Lin, H. & Thiel, W. Green fluorescent proteins: empirical force field for the neutral and deprotonated forms of the chromophore. Molecular dynamics simulations of the wild type and S65T mutant. *Journal of Physical Chemistry B* **106**, 6310-6321 (2002).
12. Beroza, P., Fredkin, D.R., Okamura, M.Y. & Feher, G. Protonation of interacting residues in a protein by a Monte Carlo method: application to lysozyme and the photosynthetic reaction center of Rhodobacter sphaeroides. *Proc Natl Acad Sci U S A* **88**, 5804-8 (1991).
13. Humphrey, W., Dalke, A. & Schulten, K. VMD: visual molecular dynamics. *J Mol Graph* **14**, 33-8, 27-8 (1996).
14. Phillips, J.C. et al. Scalable molecular dynamics with NAMD. *J Comput Chem* **26**, 1781-802 (2005).
15. Jorgensen, W.L., Chandrasekhar, J., Madura, J.D., Impey, R.W. & Klein, M.L. Comparison of simple potential functions for simulating liquid water. . *Journal of Chemical Physics* **79**, 926-935 (1983).
16. Neese, F. & The ORCA program system. Wiley Interdisciplinary Review of Computational Molecular Science. **2**, 73-78 (2011).
17. Lelimousin, M., Adam, V., Nienhaus, G.U., Bourgeois, D. & Field, M.J. Photoconversion of the fluorescent protein EosFP: a hybrid potential simulation study reveals intersystem crossings. *J Am Chem Soc* **131**, 16814-23 (2009).

18. Roy, A., Field, M.J., Adam, V. & Bourgeois, D. The nature of transient dark states in a photoactivatable fluorescent protein. *J Am Chem Soc* **133**, 18586-9 (2011).
19. Dewar, M.J.S., Zoebisch, E.G., Healy, E.F., Stewart, J.J.P. & AM1: a new general purpose quantum mechanical molecular model. *Journal of the American Chemical Society* **107**, 3902-3909 (1985).
20. Slavicek, P. & Martinez, T.J. Ab initio floating occupation molecular orbital-complete active space configuration interaction: an efficient approximation to CASSCF. *J Chem Phys* **132**, 234102 (2010).
21. Polyakov, I.V., Grigorenko, B.L., Epifanovsky, E.M., Krylov, A.I. & Nemukhin, A.V. Potential Energy Landscape of the Electronic States of the GFP Chromophore in Different Protonation Forms: Electronic Transition Energies and Conical Intersections. *J Chem Theory Comput* **6**, 2377-87 (2010).
22. Wanko, M., Garcia-Risueno, P., Rubio, A. & Excited states of the green fluorescent protein chromophore: Performance of ab initio and semi-empirical methods. *Physica Status Solidi B* **249**, 392-400 (2012).
23. Field, M.J. A molecular dynamics simulation of photo-induced electron transfer in an organic donor-acceptor compound. *Chemical Physics Letters* **195**, 388-392 (1992).
24. Fabiano, E., Groenhof, G. & Thiel, W. Approximate switching algorithms for trajectory surface hopping. *Chemical Physics* **351**, 111-116 (2008).
25. Frisch, M.J. et al. Gaussian 03, Revision C.02. (2003).
26. Case, D.A. et al. AMBER 10. 10 edn (University of California, San Francisco, 2008).
27. Jonasson, G. et al. Excited State Dynamics of the Green Fluorescent Protein on the Nanosecond Time Scale. *J Chem Theory Comput* **7**, 1990-7 (2011).
28. Filippi, C., Zaccheddu, M. & Buda, F. Absorption Spectrum of the Green Fluorescent Protein Chromophore: A Difficult Case for ab Initio Methods? *Journal of Chemical Theory and Computation* **5**, 2074-2087 (2009).
29. Toniolo, A., Olsen, S., Manohar, L. & Martinez, T.J. Conical intersection dynamics in solution: the chromophore of Green Fluorescent Protein. *Faraday Discuss* **127**, 149-63 (2004).
30. Olsen, S., Lamothe, K. & Martinez, T.J. Protonic gating of excited-state twisting and charge localization in GFP chromophores: a mechanistic hypothesis for reversible photoswitching. *J Am Chem Soc* **132**, 1192-3 (2010).
31. Jonasson, G., PhD thesis, Etude théorique de l'extinction de fluorescence des protéines fluorescentes : champ de forces, mécanisme moléculaire et modèle cinétique, Université Paris-Sud (2012).
32. A.M. Koster, P. Calaminici, M.E. Casida, V.D. Dominguez, Flores-Moreno, G. Geudtner, A. Goursot, T. Heine, A. Ipatov, F. Janetzko, J.M. del Campo, J.U. Reveles, A. Vela, B. Zuniga and D.R. Salahub, deMon2k, Version 2, The deMon developers, Cinvestav, Mexico City (2006).
33. Grotjohann, T. et al. rsEGFP2 enables fast RESOLFT nanoscopy of living cells. *eLife* **1**, e00248 (2012).
34. El Khatib, M., Martins, A., Bourgeois, D., Colletier, J.P. & Adam, V. Rational design of ultrastable and reversibly photoswitchable fluorescent proteins for super-resolution imaging of the bacterial periplasm. *Sci Rep* **6**, 18459 (2016).
35. Lomb, L. et al. An anti-settling sample delivery instrument for serial femtosecond crystallography. *Journal of Applied Crystallography* **45**, 674-678 (2012).
36. Liang, M. et al. The Coherent X-ray Imaging instrument at the Linac Coherent Light Source. *J. Synchrotron Rad.* **22**, 514-519 (2015).

37. Weierstall, U., Spence, J.C. & Doak, R.B. Injector for scattering measurements on fully solvated biospecies. *Rev Sci Instrum* **83**, 035108 (2012).
38. Schiro, G., Woodhouse, J., Weik, M., Schlichting, I. & Shoeman, R.L. Simple and efficient system for photoconverting light-sensitive proteins in serial crystallography experiments. *Journal of Applied Crystallography* **50**, 932-939 (2017).
39. Blaj, G. et al. X-ray detectors at the Linac Coherent Light Source. *Journal of Synchrotron Radiation* **22**, 577-583 (2015).
40. Foucar, L. et al. CASS-CFEL-ASG software suite. *Computer Physics Communications* **183**, 2207-2213 (2012).
41. Foucar, L. CFEL-ASG Software Suite (CASS): usage for free-electron laser experiments with biological focus. *Journal of Applied Crystallography* **49**, 1336-1346 (2016).
42. Barends, T.R. et al. Direct observation of ultrafast collective motions in CO myoglobin upon ligand dissociation. *Science* **350**, 445-50 (2015).
43. Zeldin, O.B., Brockhauser, S., Bremridge, J., Holton, J.M. & Garman, E.F. Predicting the X-ray lifetime of protein crystals. *Proc Natl Acad Sci U S A* **110**, 20551-6 (2013).
44. Zeldin, O.B., Gerstel, M. & Garman, E.F. RADDOSE-3D: time- and space-resolved modelling of dose in macromolecular crystallography. *Journal of Applied Crystallography* **46**, 1225-1230 (2013).
45. Harmand, M. et al. Achieving few-femtosecond time-sorting at hard X-ray free-electron lasers. *Nature Photonics* **7**, 215-218 (2013).
46. Coquelle, N. et al. Raster-scanning serial protein crystallography using micro- and nano-focused synchrotron beams. *Acta Crystallographica Section D Biological Crystallography* **71**, 1184-1196 (2015).
47. White, T.A. et al. Crystallographic data processing for free-electron laser sources. *Acta Crystallogr D Biol Crystallogr.* **69**, 1231-1240 (2013).
48. Nass, K. et al. Protein structure determination by single-wavelength anomalous diffraction phasing of X-ray free-electron laser data. *IUCrJ* **3**, 180-91 (2016).
49. McCoy, A.J. et al. Phaser crystallographic software. *Journal of Applied Crystallography* **40**, 658-674 (2007).
50. Adams, P.D. et al. PHENIX: a comprehensive Python-based system for macromolecular structure solution. *Acta Crystallographica. Section D, Biological Crystallography* **66**, 213-221 (2010).
51. Emsley, P. & Cowtan, K. Coot: model-building tools for molecular graphics. *Acta Crystallographica. Section D, Biological Crystallography* **60**, 2126-2132 (2004).
52. The PyMOL Molecular Graphics System. 1.5.0.4 edn (Schrödinger, LLC.).
53. Hunter, J.D. Matplotlib: A 2D Graphics Environment. *Computing in Science & Engineering* **9**, 90-95 (2007).
54. Ursby, T. & Bourgeois, D. Improved Estimation of Structure-Factor Difference Amplitudesfrom Poorly Accurate Data. *Acta Crystallographica Section A Foundations of Crystallography* **53**, 564-575 (1997).
55. Brunger, A.T. Version 1.2 of the Crystallography and NMR system. *Nature Protocols* **2**, 2728-2733 (2007).
56. Colletier, J.-P. et al. Shoot-and-Trap: Use of specific x-ray damage to study structural protein dynamics by temperature-controlled cryo-crystallography. *Proceedings of the National Academy of Sciences* **105**, 11742-11747 (2008).

57. Terwilliger, T.C. & Berendzen, J. Difference refinement: obtaining differences between two related structures. *Acta Crystallogr D Biol Crystallogr.* **51**, 609-18. (1995).
58. Colletier, J.-P. et al. Use of a `caged' analogue to study the traffic of choline within acetylcholinesterase by kinetic crystallography. *Acta Crystallographica Section D* **63**, 1115-1128 (2007).
59. Duan, C. et al. Structural evidence for a two-regime photobleaching mechanism in a reversibly switchable fluorescent protein. *J Am Chem Soc* **135**, 15841-50 (2013).
60. Colletier, J.P. et al. De novo phasing with X-ray laser reveals mosquito larvicide BinAB structure. *Nature* **539**, 43-47 (2016).
61. Schlichting, I. & Chu, K. Trapping intermediates in the crystal: ligand binding to myoglobin. *Curr Opin Struct Biol* **10**, 744-52 (2000).
62. Terwilliger, T.C. & Berendzen, J. Bayesian difference refinement. *Acta Crystallogr D Biol Crystallogr* **52**, 1004-11 (1996).
63. Duan, C. et al. Rational design of enhanced photoresistance in a photoswitchable fluorescent protein. *Methods and Applications in Fluorescence* **3**, 014004 (2015).
64. Ward, W.W. Properties of the coelenterate green-fluorescent proteins. in *Bioluminescence and chemiluminescence: basic chemistry and analytical applications* (ed. DeLuca M. A., M.W.D.) (Academic Press 1981).
65. Winn, M.D. et al. Overview of the CCP4 suite and current developments. *Acta Crystallogr D Biol Crystallogr* **67**, 235-42 (2011).
66. White, T.A. Post-refinement method for snapshot serial crystallography. *Philos Trans R Soc Lond B Biol Sci* **369**, 20130330 (2014).